Title
Terahertz time-domain characterization of amplifying quantum cascade metasurface

Author
Shen, Yue

Publication Date
2019

Peer reviewed|Thesis/dissertation

UNIVERSITY OF CALIFORNIA

Los Angeles

Terahertz time-domain characterization of amplifying quantum cascade metasurface

A thesis submitted in partial satisfaction

of the requirements for the degree Master of Science

in Electrical & Computer Engineering

by

Yue Shen

2019

ABSTRACT OF THE THESIS

Terahertz time-domain characterization of amplifying quantum cascade metasurface

by

Yue Shen

Master of Science in Electrical & Computer Engineering

University of California, Los Angeles, 2019

Professor Benjamin S. Williams, Chair

The THz quantum-cascade vertical-external-cavity surface-emitting-laser (QC-VECSEL) is a recently developed approach for designing high-power, electrically pumped THz lasers with excellent beam quality and broadband tunability. The key component of the QC-VECSEL is an amplifying reflectarray metasurface, based on a subwavelength array of surface radiating metal-metal waveguide antenna elements loaded with QC-laser gain material. Despite its importance, the gain properties of the QC-metasurface are designed by simulation and have only been verified indirectly through observation of the QC-VECSEL lasing characteristics, or by passive FTIR

reflectance measurements at room-temperature. THz time-domain spectroscopy (TDS) has been widely used to investigate gain spectra and laser dynamics of THz QC-lasers based on various ridge waveguide geometries. In this thesis, I describe my construction of a THz TDS system and present the first direct spectral measurement using reflection-mode THz TDS of an amplifying QC-metasurface resonant at 2.6 THz under different conditions. The large surface-radiating aperture of the metasurface ($1.5\times1.5\ mm^2$ in this case) eases free-space TDS measurements compared to ridge waveguide QC-devices with sub-wavelength sized facets.

The thesis of Yue Shen is approved.

Mona Jarrahi

Tatsuo Itoh

Benjamin S. Williams, Committee Chair

University of California, Los Angeles

2019

To my parents Tongsheng Shen and Yanhong Zhou and my girlfriend Qingyang Liu whose support means a lot to me.

Table of Contents

Table of Figures

ACHKNOWLEDGMENTS

I would like to thank my advisor, Professor Benjamin Williams, for his patient guidance on this project and for teaching me the way to do research. I want to thank Christopher Curwen for sharing his thoughts and ideas with me during my research. Those discussions about the solutions to the obstacles have been helping me a lot in solving problems. I also want to thank Luyao Xu for helping me get started with the project. I also want to show my appreciation to Nezih Tolga Yardimci from Prof. Jarrahi's lab for sharing the valuable experience with me about the TDS system. Finally, I want to thank Qi-Sheng Chen from Northrop Grumman Aerospace Systems for epitaxial growth of the QC-laser material.

Chapter 1: Introduction

1.1 Background on TDS of QCLs

Since the first terahertz (THz) quantum cascade laser (QCL) was demonstrated in 2002[1], considerable research has been conducted in the recent 20 years to produce rapid evolution, making QCL a significant source with milliwatt-level or higher output power in 1.2-5.6 THz frequency range[2–6]. Surface plasmon and metal-metal (MM) waveguides are two major classes for waveguide design of QCL. The surface plasmon waveguides have a thin (0.2 – 0.8 μm) heavily doped layer between the active region with a metal contact on top and the semi-insulating GaAs substrate. The surface plasmon mode is bound to the top metal contact and the lower thin plasma layer. Even though the mode extends considerably into the substrate, the free carrier loss can still be minimized because of the small thickness of the heavily doped layer. Also due to mode's extension into the substrate, the confinement factor Γ, which describes the overlap of the mode with the active region, is in low range (0.1 – 0.5). In comparison, MM waveguides have the active region between two metal layers separated by ~10 μm. As a result, the mode is almost completely confined to the active region ($\Gamma \approx 1$). Since the free space wavelength is about 100 μm, the subwavelength mode has an impedance mismatch with the free space propagating mode, which causes higher reflectance at the facet, but allows smaller threshold current densities and higher operating temperatures. However, the subwavelength nature of the modes in the MM waveguides also brings poor beam patterns and low output powers. In summary, MM waveguides tend to have better temperature performance while surface plasmon ones have higher output powers and better beam patterns[2].

To realize further performance improvements and develop better understanding of the fundamental mechanisms of QCL operation, detailed measurements are needed to characterize the gain and loss characteristics of QCLs. By relying on generation of phase-locked THz pulses driven by a femtosecond laser and coherent detection of the THz electric field, THz time domain spectroscopy (TDS)[7–9] is a powerful technique to measure the gain spectra in QCLs[10–17] . Unlike incoherent techniques like Fourier Transform spectroscopy, THz TDS can coherently characterize both amplitude and phase spectra. After the first gain spectra were obtained for bound-to-continuum designs[10], following work was carried out including demonstration of longitudinal spatial hole burning effect[11], investigation of gain as a function of different operating conditions[12], and spectral gain narrowing with increasing current density[13]. The first gain spectra for phonon-depopulation based QCLs was demonstrated later[14]. All the early TDS experiments mentioned above were performed on QCLs that employ surface plasmon waveguides. This is partially due to the efficient coupling of free space THz pulses into the large mode associated with surface plasmon waveguides. In comparison, the coupling efficiency decreases drastically for MM waveguides due to the sub-wavelength transverse dimension. This presents a problem for studying MM waveguide QCLs using THz TDS, since the free-space THz pulse must be coupled into the waveguide through this sub-wavelength sized facet. Several schemes have been proposed to overcome the coupling efficiency challenge for TDS investigation, including horn antennae[18], affixed silicon hyper hemispherical lenses[19] and gratings[20]. Design of a THz pulse emitter monolithically integrated with a QCL has been the most successful solution for TDS study of MM waveguide QCLs[16,17]. The THz emitter is separated from QCL section with a gap of ~ 4 μm wide by lithographically etching the QCL ridge. The emitter acts as a photoconductive switch with the QCL gain medium to generate broadband THz pulses that are fed directly into the MM waveguide laser cavity. The

same configuration for both emitter and QCL and the small width of the gap will contribute to higher coupling efficiency. Coupling THz pulses into the waveguides is the major challenge for edge emitting QCL. In comparison, the surface-emitting THz VECSEL that we are investigating (described in detail below) avoid the entire coupling problem as we are shining THz radiation onto a metasurface, which has a much larger area (~1 mm side length) than facet area of MM waveguide (~10 μm transverse size).

Besides characterization of quantum cascade gain media, TDS has also been used to measure the electric field of THz QCL emission by injection seeding a QCL with coherent THz pulse generated via femtosecond laser[21]. Carrier phase of laser emission is forced to lock with each femtosecond laser pulse in this way, which enables observation of the buildup of the laser field from initiation to the steady state and gives insight into laser dynamics. In addition, QCL has been demonstrated as an integrated source and amplifier for a TDS system based on injection seeding[22,23] where gain switching of QCL is used to achieve unclamped amplification[24] and the coupled-cavity scheme of MM waveguide[16,17] helps to increase coupling efficiency. Related research like sampling coherence measurements[25] and selection/suppression of longitudinal modes with narrow-band injection seeding[26] help to understand the mechanisms better.

Because of its potential applications in spectroscopy, mode locking of QCL has received significant attention and was demonstrated in mid-IR first in 2009[27]. Active mode locking of QCL in THz spectral range was demonstrated in 2011 by modulating bias current at round trip frequency[28]. Detection relies on asynchronous sampling by phase-locking the QCL source to femtosecond laser pulse. Intensity sampling scheme is also utilized to measure the mode locked THz pulses without need for stabilization electronics[29], however the measurement has no

information on carrier-envelope phase. Another solution to achieve mode locking is based on direct control over individual phases of longitudinal modes via injection seeding[30]. By combining phase seeding[30] and round trip modulation of QCL[28,29], we have the access to the field profile, amplitude and phase of each cavity mode which will help us to study dynamics of mode locking[31]. Dispersion compensation challenge for mode locked QCL can be solved by using a coupled cavity resonator that acts as an Gires-Tournois interferometer[32].

1.2 Background on VECSEL

A traditional vertical-external-cavity surface-emitting-laser (VECSEL) is semiconductor laser based on optically or electrically pumped surface-emitting semiconductor and a laser resonator completed with one or more external optical elements[33–36]. The surface-emitting semiconductor has the basic configuration of gain medium backed by distributed Bragg reflector (DBR). VECSELs can generate laser beams with a combination of high output power and near-diffraction-limited beam quality[35]. As is stated before, realization of both high power and high-quality beam pattern in one device is a problem for THz QCL because of the subwavelength metallic waveguides[37]. To address this issue, VECSEL was first demonstrated in THz spectral region for QCL and was named QC-VECSEL[38] (Figure 1.1a). The issue that "intersubband selection rule" limits implementation of QC-VECSEL can be addressed by developing the active reflectarray metasurface. The reflectarray metasurface is based on a subwavelength array of surface radiating metal-metal waveguide antenna elements loaded with QC-laser gain material (Figure 1.1b). Free-space THz radiation is coupled into the metasurface and reradiated after getting amplified in gain medium. In addition, broadband tunability of phase, amplitude and polarization response of the

metasurface enables QC-VECSEL with new functionality[38–40], like higher beam quality with focusing metasurface[39] and electrically switchable polarization design[40].

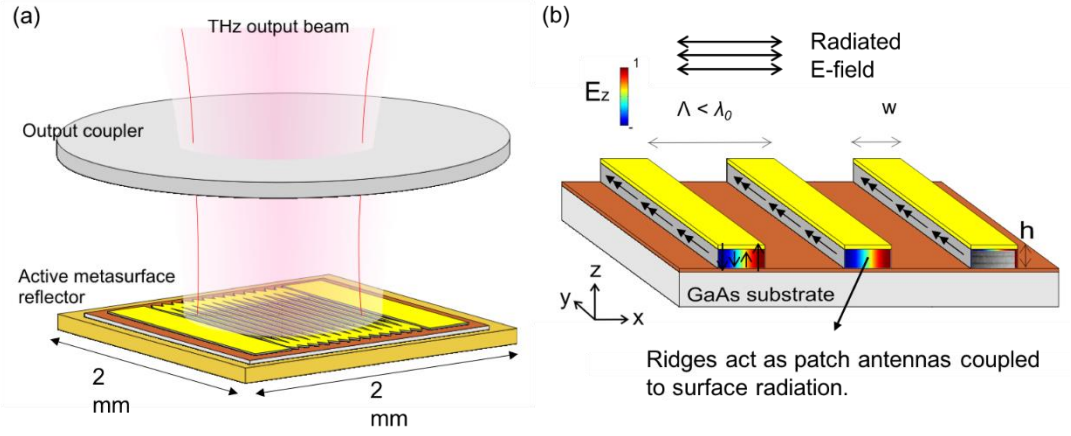

Figure 1.1 (a) Illustration of QC-VECSEL configuration including the active metasurface and output coupler. (b) Schematic of reflectarray.

Chapter 2: Theory, Design and Calibration of THz Time-Domain Spectroscopy

2.1 Background on THz time-domain spectroscopy

The THz region, with frequencies generally defined in the range from 300 GHz to 10 THz (see Figure 2.1), hosts a wealth of intriguing properties and potential applications including but not limited to astrophysics and atmospheric science, biomedical science, security screening, industrial control, telecommunications and spectroscopy[2,41]. THz beams can propagate through some optically opaque materials while the radiation is non-destructive and non-ionizing. Furthermore, THz radiation can interact strongly with different matter in physical, chemical and biological systems. These properties make THz spectroscopy a promising tool for characterizing rotational and vibrational resonances[42], excitons[43–45], phonons in crystalline solids[46], hydrated biological matter and other different phenomena[47,48]. In addition, THz spectroscopy allows for characterization of THz devices, like THz filters[49], dielectric mirrors[50,51] and wave guides[50,51].

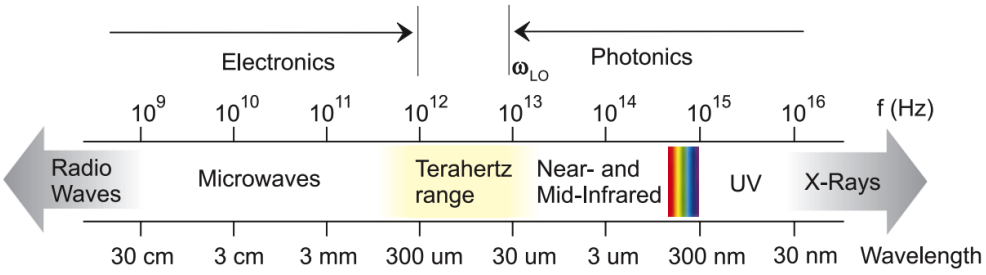

Figure 2.1 Diagram of terahertz spectrum (This figure courtesy of Ref. 2).

Fourier transform infrared (FTIR) spectroscopy as the first form of spectroscopy in far-infrared regime was introduced in 1950s[52]. It can be used to study samples with help of Michelson interferometer. The basic operation in Fourier transform spectroscopy is a two-beam interferometry. The broadband beam is divided into two parts. The sample is transmitted with beam in one arm while the path length of the other arm is varied to give a phase change. The detector can measure the frequency integral of squared amplitudes to generate interferogram. And Fourier transform can convert the interferogram into spectrum. THz TDS, as an alternative method for spectroscopy, was first described in 1989 following the development of femtosecond lasers and photoconductive dipole antennas[53]. Compared with FTIR, TDS has higher SNR and wider dynamic range in a synchronous and coherent manner[54]. Moreover, as its electric field itself is measured instead of intensity, the amplitude and phase spectrum can be determined after one single scan. Thus, the complex permittivity of the sample can be deduced via TDS without resorting to Kramers-Kronig analysis[53]. THz TDS technology has been playing important role in pharmaceutical applications, material studies, medical applications, security area and many other areas.

2.2 Setup design and theory of TDS

2.2.1 The setup of THz-TDS

The first primary part of my MS thesis was the construction of a THz TDS system customized to allow characterization of our QC-metasurfaces. The setup of a generic transmission-mode THz-TDS system is shown in Figure 2.2. As we are investigating QC-VECSEL reflectarray metasurfaces, which do not transmit radiation, its surface emitting property will require reflection-

mode spectroscopy. With help of reflection-mode TDS system, we can study the gain and loss spectra of the QC-metasurface by directing THz pulse onto the reflectarray and collecting the reradiated pulse. The advantage of the design of this setup is that it can be switched between two modes (transmission and reflection) with the minimal effort, just by adding/removing a THz beam splitter and a mirror into/from the setup. I began by building the transmission-mode system, and after making sure the spectroscopy generated by the system met our requirements, I moved on to realize the reflection-mode setup whose schematics are shown in the following chapters (see Figure 3.2).

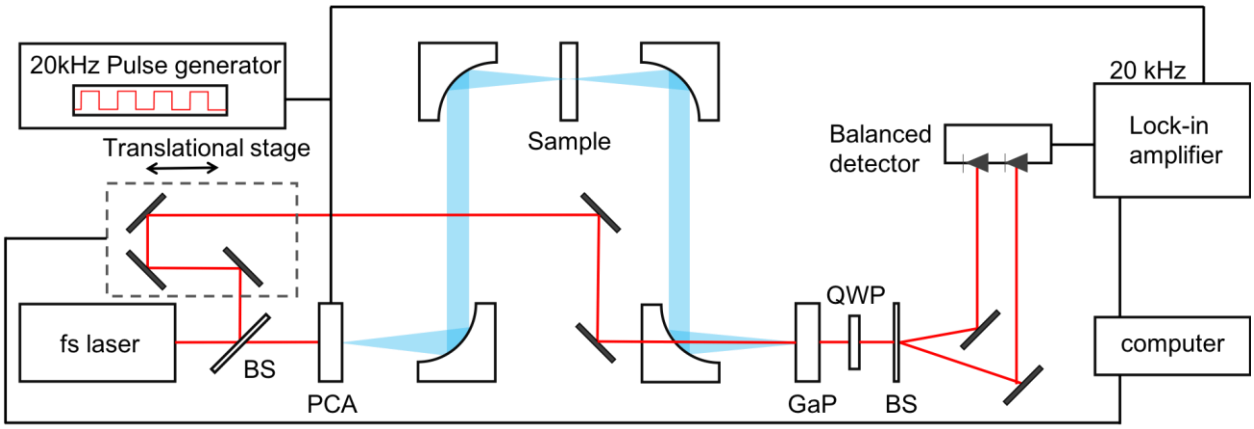

Figure 2.2 The schematic diagram of THz-TDS transmission-mode system.

As stated in the background of TDS, the whole system relies on the use of an ultrafast mode-locked laser, usually a Ti:sapphire laser or fiber laser that can produce light pulses with duration from 10 to 150 fs. The laser beam is divided into a probe beam and a pump beam. The pump beam is directed to the THz emitter (photoconductive antenna in our setup) to generate the THz transient of ~1 ps duration with a broadband coverage in THz region. The THz signal will arrive at the THz detector (nonlinear crystal in our setup) guided by several off-axis parabolic mirrors, while the probe beam will also be directed onto THz detector at the same time by adjusting its optical path.

The optical path of the probe beam can be varied by controlling the translational stage, which allow us to change the relative arrival time between terahertz transient and optical pulse to the detector. As the duration of the optical pulse is much smaller than time scale of THz transient, the signal produced by the detector will be proportional to the instantaneous electric field of THz signal. By sweeping the translational stage, we can map out the electric field of THz pulse as a function of time. Furthermore, we can also get the amplitude and phase spectra of THz pulse by applying Fourier transformation.

The system is mainly composed of THz emitter and THz detector, which will be discussed later. As same as the other real systems, noise needs to be considered and analyzed, which will also appear in the following subsections.

2.2.2 THz source

After the introduction of mode-locked pulsed laser, generation of broadband THz radiation was first realized with short carrier lifetime semiconductor based photoconductive antenna (PCA) in the late 1980s by the research groups of David Auston[7,55,56] and Daniel Grischkowsky[53,57–59]. A few years later, nonlinear crystals were also demonstrated to generate THz transient as an alternative method based on electro-optic rectification[60]. Both ways to generate THz transients have developed a lot in the past decades, like to broaden the bandwidth or to increase the THz power[61–63]. I use a PCA as the THz emitter for my system because it can be electrically modulated at high frequency (20 kHz or even higher). The tradeoff is the relatively lower THz power and narrower bandwidth compared to nonlinear crystal as emitter.

A PCA is a device made up of two metallic contacts on a semiconductor substrate. The process of generating THz radiation by shining input femtosecond laser pulse onto PCA is illustrated in Figure 2.3a[64]. When the bias voltage is applied between the metallic contacts without laser pulse shone onto the semiconductor, the generated current is negligible because of the high resistivity of the semiconductor. However, when ultrafast laser pulse is incident onto the antenna gap between the contacts, photons with enough energy will excite electrons into conduction band, thus photocurrent will be excited within the antenna on a sub-picosecond time scale. In certain materials (such as low-temperature grown GaAs), the sub-ps carrier lifetime leads to the decrease of photocarriers on a sub-picosecond time scale because of recombination, trapping or momentum scattering of the carriers. As a result, the photocurrent formed by the accelerated photocarriers will also experience the increase and decrease process (shown in Figure 2.3b), thus will generate free space wave radiating in THz frequency.

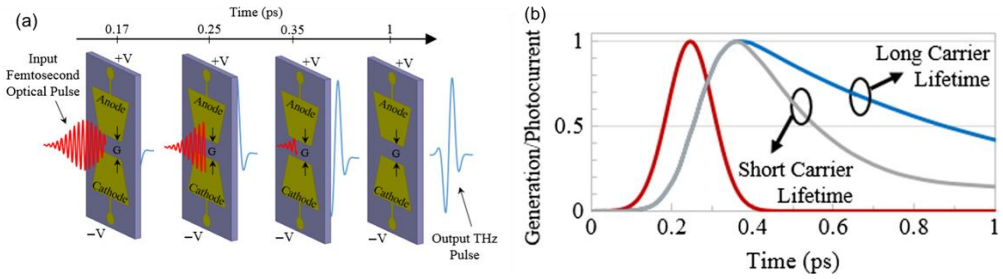

Figure 2.3 (a) The time evolution of generation of THz transient signal by shining ultrafast optical pulse onto the PCA (red wave indicates optical pulse and blue wave indicates THz pulse) (This figure courtesy of Ref. 64). (b) The carrier generation rate (red trace) and photocurrent for material of short-carrier lifetime (gray trace) and long carrier lifetime (blue trace) as a function of time (This figure courtesy of Ref. 64).

The relationship between Electric field of THz transient and the photocurrents can be explained by treating the photoconductive emitter as a dipole antenna. The electric field component perpendicular to the observation direction of an electric dipole, E_θ, can be expressed by[65]

$$E_\theta(r,\theta,t) = \frac{1}{4\pi\varepsilon_0}\left[\frac{1}{r^3}\vec{p}(t_r) + \frac{1}{cr^2}\dot{\vec{p}}(t_r) + \frac{1}{c^2 r}\ddot{\vec{p}}(t_r)\right] sin\,\theta\,, \tag{2.1}$$

where $\vec{p}$ is the electric dipole moment, r is the distance between dipole and observation position, $t_r = t - {}^{r}/_{c}$ is the retarded time and θ is the angle between direction of dipole vector and direction of observation point. In far field approximation, only the third term in Equation 2.1 is left. So, the E-field of far field THz transient is proportional to the second temporal derivative of dipole moment, which is first temporal derivative of photocurrent

$$E_{THz}(t) \propto \frac{\partial J_{ph}}{\partial t}. \tag{2.2}$$

We can verify this relationship by comparing the THz pulse shape in Figure 2.3a (blue wave) and the photocurrent as a function of time in Figure 2-2b (grey or blue curve). Drude model can be used to explain the feature of carriers and photocurrents of the semiconductor[61]. This model can predict many features of the THz transient and help us to choose appropriate material and experimental settings to broaden the bandwidth of THz pulse despite its simplicity. If the semiconductor has a long carrier lifetime, the photocarriers will contribute to form photocurrent for a long time after the photons are absorbed, which will cause the decay of photocurrents to be in long time scale. The semiconductor with shorter carrier lifetime will have the opposite effect[61,66,67]. Shortening of the pulse of photocurrent will result in shortening of pulse of THz transient in time domain, which will broaden the bandwidth of THz transient. Thus, we prefer to use material with lower carrier lifetime as the substrate of the PCA. The photocurrent can be given

by $J_{ph}(t) = -en(t)v(t)$, where $n(t)$ is density of photocarriers and $v(t)$ is the averaged velocity of the photocarriers. The velocity can be described with Drude model $\frac{dv(t)}{dt} = -\frac{v(t)}{\tau_s} + \frac{e}{m^*}E_{loc}(t)$, where τ_s is the scattering time, m^* is the effective mass and E_{loc} is the local electric field between the gap of antenna. The local electric field is sum of DC bias field E_{bias} and screening field caused by polarization P_{sc} of photocarriers, $E_{loc}(t) = E_{bias}(t) - \frac{P_{sc}(t)}{\eta\varepsilon}$, where η is screening factor and ε is permittivity of the material. With high excitation intensities, the bias field will be screened completely by the polarization field within sub-picosecond time scale, causing the velocity of photocarriers and thus photocurrent to decrease in sub-picosecond time scale. Photocurrents will decay slowly with low excitation intensities. As a result, we need to make sure the excitation intensity is enough to generate broadband radiation.

GaAs has been the preferred material for PCA in a long time. With bandgap 1.424 eV at room temperature, it is highly compatible photoexcitation of carriers using a Ti:Sapphire laser. As the effects of GaAs growth temperature on carrier lifetime and other PCA properties are studied, LT-GaAs, gallium arsenide grown epitaxially at low temperatures between 200°C and 250°C, is considered to possess more benefits[68–70]. Growth of GaAs in lower temperature range results in the higher level of crystallinity, which leads to higher carrier mobility. Moreover, excess As^{3+} inside the crystal structure are point defects, which act as recombination center to reduce the carrier lifetime. Carrier lifetime below 400 fs is reported with LT-GaAs grown at 190°C[70]. These properties of LT-GaAs render higher bandwidth of the radiated THz pulse. In addition, it is demonstrated that LT-GaAs based emitter generates lower photocurrent than GaAs based

counterpart to deliver similar output power[70]. Lower photocurrent means fewer thermal effects coming from high optical power and high voltage bias.

Contact geometry also plays an important role in THz pulse generation as it defines the efficiency of THz generation and coupling between free space electromagnetic field and photocurrents. When the laser power begins to increase, the number of photocarriers also increase which in turn causes the radiated THz power to increase, and there will be a saturation point where THz power becomes constant with optical power still increasing[70]. This saturation problem can be overcome by the design of interdigitated electrode structure[71,72]. The anode and cathode strips were interwoven with a gap of fix distance between the electrodes. The PCA we are using in the experiments is a large-area GaAs based emitter made by Laser Quantum[73]. As shown in Figure 2.4, the electrodes are processed onto the substrate using photolithography. Unidirectional photocurrents are generated when DC bias is applied across every other electrodes' pair by covering a metallization layer over every second electrode gap. The metallization layer is insulated from the electrodes by a SiO2 layer. In practical experiment, the PCA is biased with voltage of 20V with 25% duty cycle at 20 kHz, while the incident optical power is 600 mW on spot size of 300 μm.

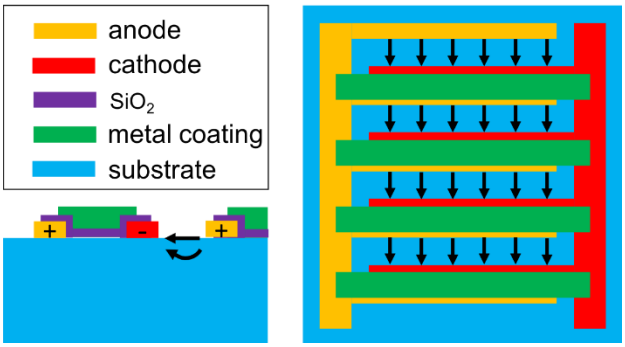

Figure 2.4 The principle layout of PCA device with cross-sectional view (left) and plane view (right).

2.2.3 THz detector

THz detection is another important part in THz TDS system. The relatively low power generated in the system together with the comparatively high thermal background radiation requires the detection to be highly sensitive. Those direct detection methods, like Schottky diodes[74], helium-cooled bolometers[75] or pyroelectric detectors, are not good choices for TDS applications. As the duty cycle of signal to be detected, the laser pulse, is at a pretty low level, while the noise is integrated from all time, the SNR is reduced by a large factor, causing the sensitivity to drop a lot. These detection methods all respond to the power of THz pulse instead of electric field, so the important phase information, which is crucial in field-matter interaction applications, is lost during detection. PCA as a detector has excellent sensitivity and far better SNR, however, its frequency response is limited by the resonant behavior of Hertzian dipole structure. The need for a detection method with high sensitivity and broadband frequency response is fulfilled by nonlinear crystal. Starting from measurements of local electric field in materials, it evolved to free space electric optic sampling (FS-EOS)[76–78] and becomes a powerful tool for THz pulse detection.

The principle of THz detection using nonlinear crystal can be explained by linear electrooptic effect (Pockel effect)[79]. THz beam can modify the index ellipsoid of the EO crystal. When optical beam propagates collinearly with THz pulse, the phase of optical beam is modulated by the refractive index modified by the electric field of the THz pulse. Phase change leads to power difference in two perpendicular polarizations, and the difference is proportional to the THz field. We can detect the power difference via balanced detector. The balanced detector not only suppresses the common noise from ultrafast laser but doubles the measured signal as well. In this way, THz electric field is revealed by the output of balanced detector.

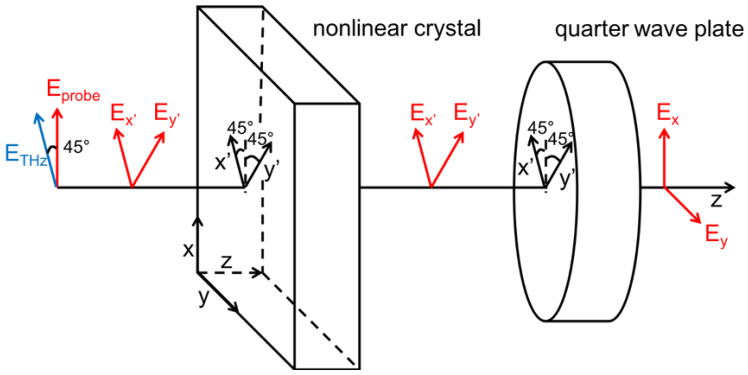

Figure 2.5 Coordinates illustration for EO sampling with $\bar{4}$3m point group nonlinear crystal, like Gap or ZnTe.

Material of zincblende structure $\bar{4}$3m point group is the major choice for nonlinear crystal, like ZnTe and GaP. Assume that THz pulse and probe pulse are propagating colinearly along z-axis, with polarization E_{probe} along x-axis and polarization E_{THz} along x'-axis, 45°with respect to x-axis. The optic axis <100> of nonlinear crystal is also along x'-axis, the fast and slow axis of the quarter wave plate are along x'-axis and y'-axis, 45°with respect to x-axis on two sides. According to Pockel effect, when linearly polarized THz electric field polarization is parallel to one optic axis of nonlinear crystal, refractive index along x'-axis remains the same while refractive index along y'-axis has a $\frac{1}{2}n^3\gamma_{41}E_{THz}$ difference from n. Given the thickness of the nonlinear crystal d and optical pulse wavelength λ, the phase difference between polarization $E_{x'}$ and $E_{y'}$ induced by E_{THz} within nonlinear crystal is

$$\Gamma = \frac{\pi d n^3 \gamma_{41}}{\lambda} E_{THz}. \tag{2.3}$$

Another phase difference between polarization $E_{x'}$ and $E_{y'}$ is accumulated when the probe beam passing through quarter wave plate. Based on the configuration of fast and slow axis mentioned

above, the additional phase difference is $\frac{\pi}{2}$. We can use Jones Matrix to calculate E_x and E_y separately,

$$\begin{pmatrix} E_x \\ E_y \end{pmatrix} = \begin{pmatrix} \cos\frac{\pi}{4} & -\sin\frac{\pi}{4} \\ \sin\frac{\pi}{4} & \cos\frac{\pi}{4} \end{pmatrix} \begin{pmatrix} e^{i\frac{\pi}{2}} & 0 \\ 0 & 1 \end{pmatrix} \begin{pmatrix} e^{i\Gamma} & 0 \\ 0 & 1 \end{pmatrix} \begin{pmatrix} \cos\frac{\pi}{4} & \sin\frac{\pi}{4} \\ -\sin\frac{\pi}{4} & \cos\frac{\pi}{4} \end{pmatrix} \begin{pmatrix} E_{probe} \\ 0 \end{pmatrix}. \tag{2.4}$$

Then we can derive the power in x and y polarization,

$$\begin{cases} I_x = |E_x|^2 = I_0 \left(\cos\dfrac{\frac{\pi}{2} + \Gamma}{2} \right)^2 \\ I_y = |E_y|^2 = I_0 \left(\sin\dfrac{\frac{\pi}{2} + \Gamma}{2} \right)^2 \end{cases} \tag{2.5}$$

As $|\Gamma| \ll 1$, the expression for I_x and I_y can be simplified,

$$\begin{cases} I_x = \dfrac{I_0}{2}(1 - \Gamma) \\ I_y = \dfrac{I_0}{2}(1 + \Gamma) \end{cases} \tag{2.6}$$

By substituting Eq. 2-3 into Eq. 2-6, we can get the relationship between the difference signal, $I_x - I_y$, and E_{THz},

$$I_s = \frac{I_0 \pi d n^3 \gamma_{41}}{\lambda} E_{THz}. \tag{2.7}$$

There is also analysis and experiments on orientation dependence of THz detection, and the conclusion is the maximum signal is achieved when angles between THz and probe beam polarizations are 0° or 90°.

The result from Equation 2.7 assumes that there is a DC bias on nonlinear crystal. For THz pulse in the real experiment, phase matching of THz pulse and optical pulse needs to be considered. For the ideal case, probe pulse travels with the same group velocity as that of THz pulse, so that the phase change of probe beam can be associated with the amplitude of THz transient at one specific position. However, as there exists a group velocity mismatch (GVM), the phase variation of probe pulse is accumulated along its propagation of the THz pulse over the length of the crystal. The scan duration, or the accumulated GVM time is

$$\delta(\Omega) = \frac{n_g(\lambda_0) - n(\Omega)}{c} d. \tag{2.8}$$

where $n_g(\lambda_0)$ is optical group index, $n(\Omega)$ is the THz refractive index. The actual bias modulating the nonlinear crystal can be regarded as the time average of the electric field of THz transient across the GVM time $\delta(\Omega)$. The frequency response function has the form as:

$$G(\Omega) = \frac{t(\Omega)}{\delta(\Omega)} \int_0^{\delta(\Omega)} e^{i2\pi\Omega t}\, dt = \frac{2}{n(\Omega)+1} \frac{e^{i2\pi\Omega\delta(\Omega)} - 1}{i2\pi\Omega\delta(\Omega)}, \tag{2.9}$$

where $t(\Omega)$ is transmission coefficient that obey Fresnel law. Figure 2.6a plots the calculated (solid line) and experimental data (open circles) of group index for optical pulse and THz pulse[80]. The frequency response function of GaP with different thickness is showed in Figure 2.6b. We can tell that with thinner crystal thickness, the frequency response extends to broader bandwidth, which is what we pursue. However, smaller thickness may lead to a weaker output difference signal as indicated in Equation 2.7, therefore smaller sensitivity. Thus, there is a tradeoff between broadband response and high sensitivity.

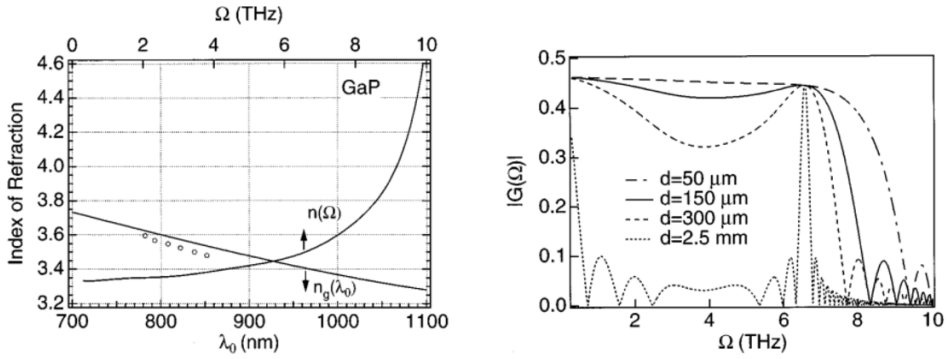

Figure 2.6 (a) Optical group index $n_g(\lambda_0)$ and THz refractive index $n(\Omega)$ in GaP (This figure courtesy of Ref. 80). (b) Frequency response function of GaP with different thickness for $n_g = 3.50$ when $\lambda_0 = 840\ nm$ (This figure courtesy of Ref. 80).

We are using GaP as the nonlinear crystal for detection because of its high phonon resonance frequency at 11 THz, compared with ZnTe at 5 THz, and moderate electrooptic coefficient, one fourth of ZnTe. The EO crystal is made up of a 300 μm <110> GaP attached onto 2 mm <100> GaP, the substrate <100> GaP doesn't have electrooptic effect and is used to increase reflection free time window. There are other different ways to improve the bandwidth of frequency response or sensitivity, like quasi-phase matching[81], angle tuning of GaSe for phase matching condition[82] or organic crystal DAST[83]. These choices may be helpful to improve the experiment results in the future.

2.2.4 Noise analysis

There are several kinds of noise associated with THz TDS system. The noise mainly come from THz detector and THz source. The major noise source from THz detector includes: (i) thermal Johnson noise generated in the resistor of balanced detector which exists independent with the probe beam, (ii) background thermal radiation and (iii) shot noise caused by photocurrent. As we have mentioned above, common-mode noise associated with fluctuation of the probe beam is

avoided by using a balanced detector. Normally shot noise is the dominant noise source for detector. The signal is proportional to probe beam power while shot noise is proportional to square root of probe beam power, thus, signal to noise ratio can be increased by increasing the probe beam power. However, research indicates that over the specific limit, higher power illumination may cause the reduction in bandwidth[84]. As the limit of power for our balanced detector is 1mW, we tried different incident power from 50 μW to 1mW and found that the optimum power is in the range from 500 μW to 1mW, where the SNR is almost constant and better than lower probe beam power scenarios, so we choose the incident power to be 500 μW. As for the noise from PCA, it is primarily caused by laser fluctuation and leads to main error on THz constant characterization. We will be covering how to suppress the noise and generate a broadband spectroscopy with high dynamic range with help of signal processing in the next section.

2.3 Experimental setting and signal processing

In this section, we will talk more about how we change the experimental settings to get the higher-quality raw data and the following signal processing steps exerted on the spectroscopy.

2.3.1 Basics of data analysis in THz processing

After acquisition of electric field of THz pulse $E(t)$, we can get the frequency information via Fourier Transform

$$E(\omega) = \frac{1}{2\pi} \int_{-\infty}^{+\infty} e^{-i\omega t}\, E(t)\, dt. \tag{2.10}$$

There are several related concepts of both $E(t)$ and $E(\omega)$, like dynamic range, signal-to-noise ratio (SNR) and spectral resolution. These aspects are important for evaluation of THz TDS measurements.

Usually dynamic range[85] refers to the spectral data, $\mathrm{E}(\omega)$. It is defined as the ratio between the largest and smallest measurable signal, and can be expressed as:

$$DR = \frac{E_{max}}{N_{rms}}, \tag{2.11}$$

where $\mathrm{E_{max}}$ is the peak magnitude in spectral data and $\mathrm{N_{rms}}$ stands for the root-mean-square of the noise floor. For better characterization of quantum-cascade metasurface in our application, we expect the dynamic range to be as high as possible. SNR reveals the minimum detectable signal change of the system. It is a reflection of amplitude resolution or sensitivity. SNR can be defined as ratio between mean magnitude of amplitude and standard deviation of amplitude, in form of

$$\mathrm{SNR} = \frac{\overline{\mathrm{E}}}{\sigma_{\mathrm{E}}}. \tag{2.12}$$

Based on the properties of Fourier Transformation, the spectral resolution of the system is given by $^{\mathrm{c}}/_{2\mathrm{L}}$, where L is the travelling range of translational stage during experiment. For noiseless unlimited range translational stage, the resolution is limited by repetition rate of femtosecond laser. Usually L is limited by the thickness of PCA and EO crystal to get the reflection-free temporal electric field, as multiple reflection may occur in semiconductor of PCA or in nonlinear crystal. For our setup, L is limited by the thickness of PCA and can reach 2.3 mm at most, which results in the spectral resolution of 65 GHz. This can be improved by adapting echoless design with a buried gold slab in the GaAs substrate in the future[86,87].

As we are collecting discrete signal for THz electric field, the Fourier Transform is Discrete Fourier Transformation (DFT). And the step size in time domain is called sampling rate. According to Nyquist sampling theorem, the continuous function $E(t)$ can be completely exchanged to the discrete data if $E(t)$ is bandwidth limited to frequencies smaller than critical frequency f_c, defined by $f_c = \frac{1}{2\Delta t}$ where Δt is the temporal step size. We set the step size to be 0.05 mm, which is 0.16 ps in time domain.

2.3.2 Purging effect

Water vapor has strong absorption of THz radiation[53], there exists several discrete absorption lines in the THz region (Figure 2.7). To avoid water absorption, we use a purging box to cover the whole space where THz pulse is propagating. By purging nitrogen gas into the purging box, the humidity can be reduced to 0.1%. Both time domain and frequency domain data with purging and without purging are shown below (Figure 2.8). We can tell that purging can reduce the absorption lines caused by water vapor for better dynamic range. The oscillations in the purging spectrum are coming from the F-P effect associated with reflections from the semiconductor substrate of the photoconductive antenna.

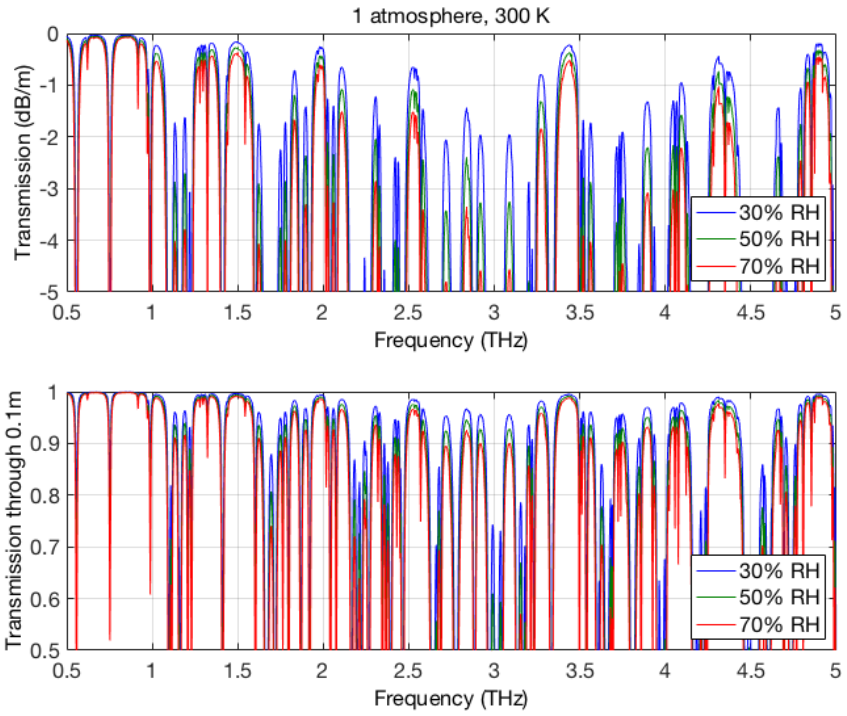

Figure 2.7 Calculated atmospheric transmission spectra under different relative humidity levels at room temperature based on the data from HITRAN database (calculation courtesy of Alan W. M. Lee).

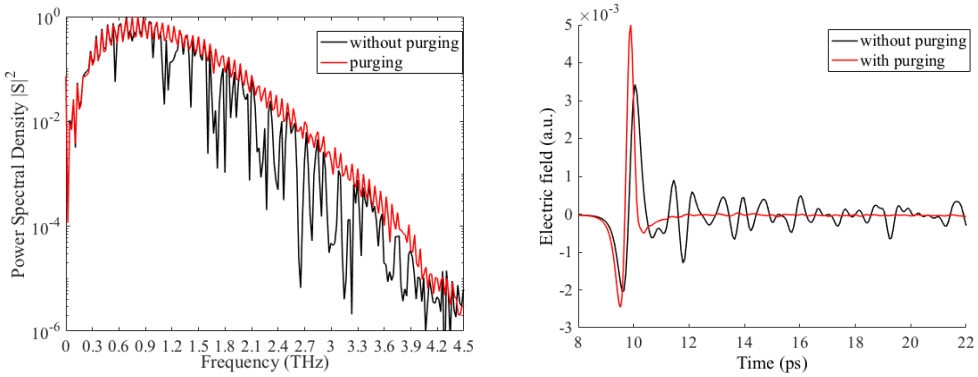

Figure 2.8 Top-view (a) Power Spectral density in frequency domain for purging and without purging configuration. (b) Electric field in time domain for purging and without purging configuration.

2.3.3 Settings of lock-in amplifier

A lock-in amplifier (Zurich Instruments MFLI) is used to measure the small AC signal even though it is obscured by noise source 3 orders higher. The amplitude of the signal is picked out by multiplying the reference signal with input signal and filtering the multiplication result with a low pass filter. Every low pass filter has its own cutoff frequency f_c, and the corresponding time-constant $\tau = \frac{1}{2\pi f_c}$. For a low time-constant, the lock-in can respond quickly to change in input signal, while the reading is pretty noisy; and for a high time-constant, the voltage reading is quite stable while it takes longer to respond to the real change in input signal. So, we need to choose the proper time constant to provide the balance between time consumption and stability. Also, we can set the number of times to read data at each position along the travel range for averaging. Averaging is the most effective way to suppress noise and increase SNR. We are using 100ms time constant and 400 times reading at each position for averaging.

2.3.4 Window function

When Fourier transform is operated without multiplying window function with the raw data of electric field, the temporal data is equivalently multiplied with a rectangular window function. The Fourier Transform of rectangular window function is a sinc function in frequency domain, which is characterized by large side-lobe levels. Multiplication of the electric field by a rectangular window function in the time domain leads to the convolution of sinc function and spectral data in frequency domain. As the sidelobe of sinc function is high, magnitude at each frequency will exert a large influence on the neighboring frequency. In order to deal with this problem, we can multiply a Hamming window with the raw data in order to reduce the influence on the magnitude of

neighboring frequency. We also need to do zero padding for the raw data to make sure the maximum value in time domain is at the middle point. Zero padding will not help with the real resolution, which works like extrapolating the original plot.

2.4 Characterization of test samples

Once the transmission mode TDS system is built, we take one silicon wafer and one output coupler used for VECSEL as the samples for characterization (setup shown in Figure 2.2). Let's assume that electromagnetic wave with amplitude $E_0(\omega)$ propagates through dielectric slab with a complex refractive index $\widetilde{n_s}$ and thickness l. Considering the Fabry-Pérot effect, we have the THz signal passing through dielectric sample expressed as

$$E_{sam}(\omega) = \eta \frac{4\widetilde{n_s}(\omega)}{[\widetilde{n_s}(\omega)+1]^2} e^{-j\widetilde{n_s}(\omega)\frac{\omega l}{c}} E_0(\omega), \tag{2.13}$$

where η represents the transmission factor of free space around the sample. Reference signal with the same setting but in absence of sample is expressed as

$$E_{ref}(\omega) = \eta e^{-j\frac{\omega l}{c}} E_0(\omega). \tag{2.14}$$

With expression of $E_{sam}(\omega)$ and $E_{ref}(\omega)$, we can deduce the transfer function $\mathrm{H}(\omega)$ of the sample through normalizing the sample spectrum by reference one:

$$\mathrm{H}(\omega) = \frac{4n_s(\omega)}{[n_s(\omega)+1]^2} e^{-\kappa_s(\omega)\frac{\omega l}{c}} e^{-[n_s(\omega)-1]\frac{\omega l}{c}}, \tag{2.15}$$

where $n_s(\omega)$ and $\kappa_s(\omega)$ are the real and imaginary part of the complex refractive index $\widetilde{n_s}(\omega)$ given by $\widetilde{n_s}(\omega) = n_s(\omega) - j\kappa_s(\omega)$.

The experimental result and the theoretical calculation are shown in Figure 2.9, we can tell that the two curves are close to each other, and the little difference may come from noise of detection and deviation of complex refractive index used in calculation.

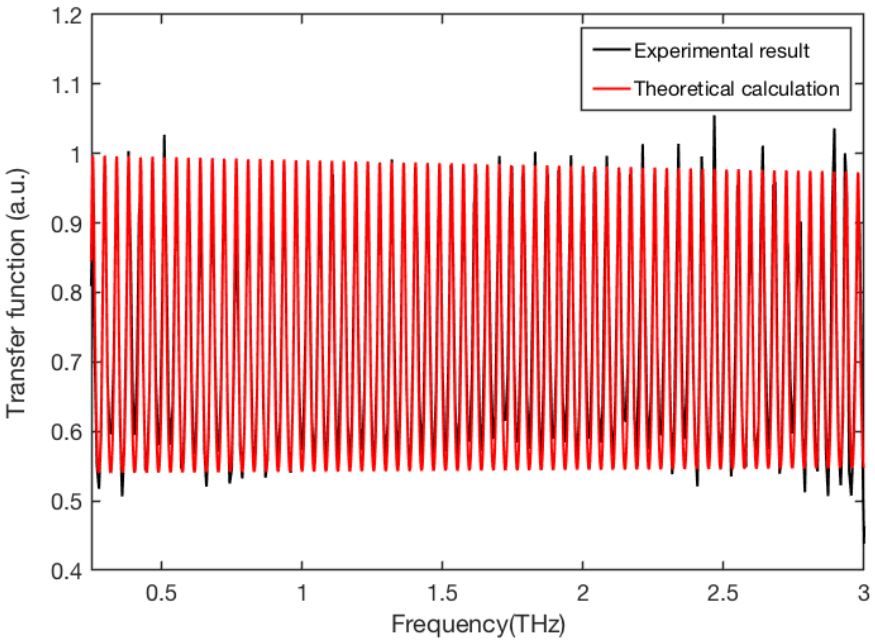

Figure 2.9 Transfer function for Si wafer sample based on experimental result and theoretical calculation.

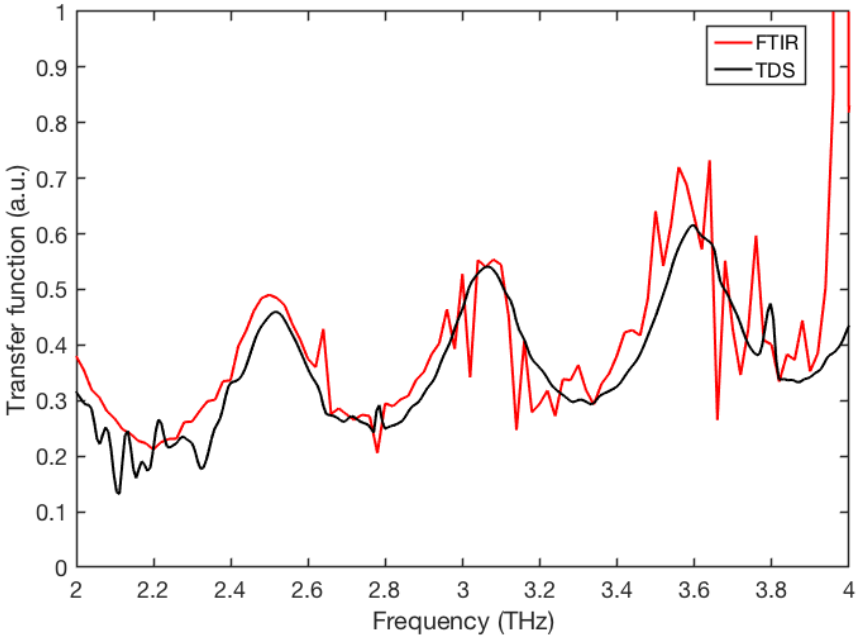

Figure 2.10 Transfer function comparison for output coupler between FTIR and TDS.

We also characterize the output coupler from a VECSEL and compare the TDS results with FTIR results as shown in Figure 2.10. The output coupler is made of z-cut crystal quartz with ~ 130 μm thickness and an evaporated Ti/Au inductive grid. The two curves fit well from 2 THz up to 3.8 THz. Those kinky spikes in the black curve may come from noise, we can tell that as the spectroscopy becomes noisier when frequency goes higher.

Chapter 3: Experiment and Simulation Results

3.1 Passive measurements of QC-metasurface

As shown in Figure 3.1a, the metasurface under investigation is composed of an array (period Λ = 90 μm) of metal-metal waveguides with ridge width $w \approx 15$ μm. Each is loaded with resonant-phonon QC-gain material exhibiting gain in the 2.4-2.7 THz range. The gain medium is resonant-phonon depopulated. The injector states are below the lower radiative state '1' by approximately E_{LO} = 36 meV, so that the electrons in lower states can quickly scatter to injector states by emitting LO-phonons[2] (Figure 3.1b). The metasurface resonance is designed for 2.6 THz, as set by the width of the ridges ($\nu_0 \approx c/2nw$) where c is the speed of light, and n is the refractive index of the semiconductor.

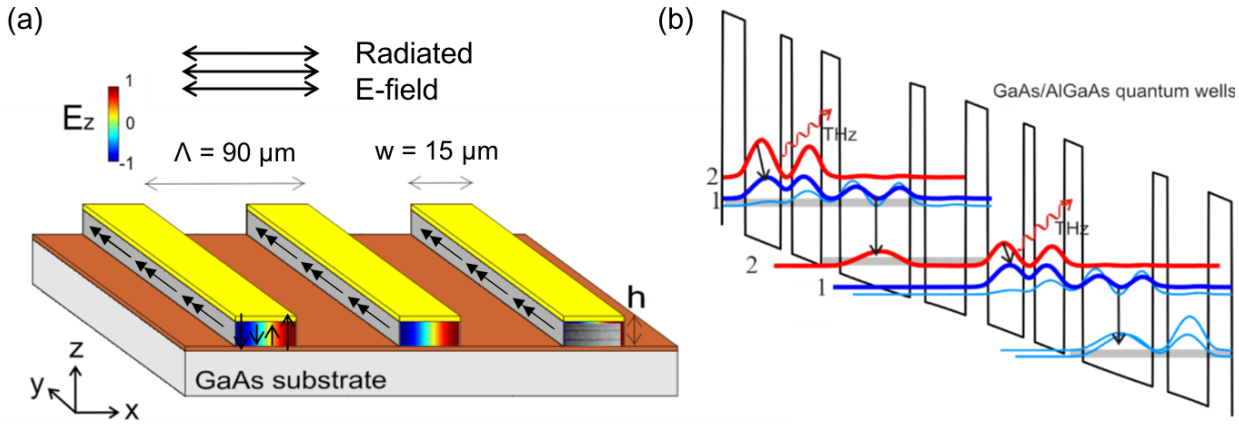

Figure 3.1 (a) Schematic of metasurface. (b) Phonon depopulation active region design.

The optical setup and electrical connection scheme are shown in Figure 3.2. The QC-metasurface as the sample is put inside a cryostat without bias, while the photoconductive antenna is modulated at 20 kHz with a duty cycle of 25%. The same signal is used for the lock-in reference. The absorption of the QC-metasurface at center frequency 2.6 THz can be revealed in the normalized spectrum by the passive measurements at room temperature (Figure 3.3). After the room temperature test, we can purge the cryostat and cool the device down to 77K to acquire the measurement results. The dip frequencies under two circumstances have a difference of 85 GHz, and this could come from change of optical path (especially the position and orientation of metasurface in the cryostat) induced by the low temperature. Also, we can tell that the dip is deeper for room temperature condition, which is reasonable as the absorption is lower for lower temperature.

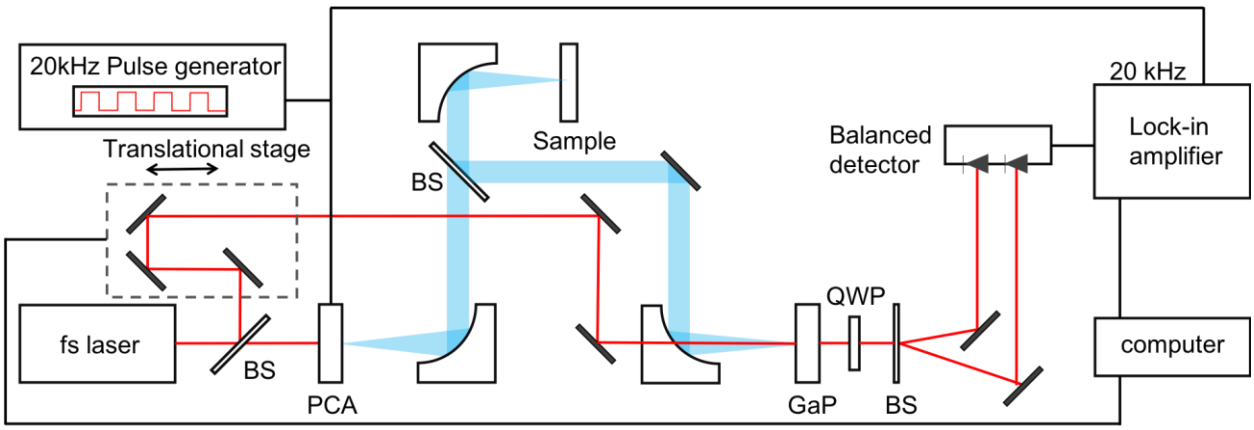

Figure 3.2 The schematic of THz TDS for passive measurements of QC-metasurface.

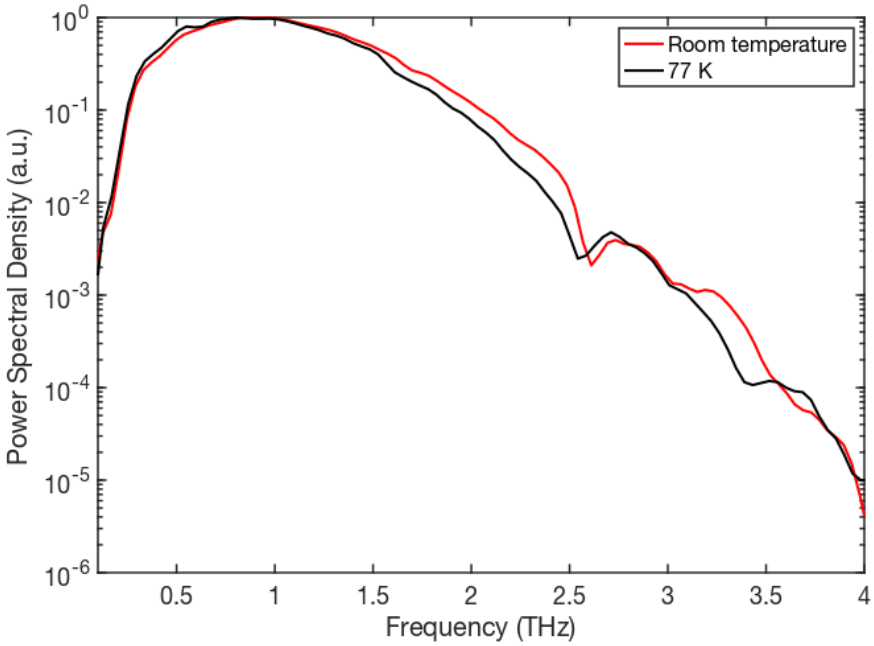

Figure 3.3 Power density of passive QC-metasurface under room temperature and 77 K (The peak value is normalized in the spectra) .

3.2 Active measurements of QC-metasurface and simulation results

The complex amplitude of the reflected field's Fourier Transform when laser is on and off can be expressed as

$$E_{on}(v) = |E_{on}(v)|\, e^{j\phi_{on}(v)}, \tag{3.1}$$

$$E_{off}(v) = \left|E_{off}(v)\right| e^{j\phi_{off}(v)}. \tag{3.2}$$

And the division of $E_{on}(v)$ over $E_{off}(v)$ can be written as

$$\left|\frac{E_{on}(v)}{E_{off}(v)}\right|^2 = \frac{e^{\xi(v)(g(v)-g_{tr}(v))}}{e^{-\xi(v)g_{tr}(v)}} = e^{\xi(v)g(v)}, \tag{3.3}$$

where $g(\upsilon)$ represents gain, $g_{tr}(\upsilon)$ is the transparency gain coefficient needed to balance absorption losses and $\xi(\upsilon)$ is fitting coefficient correlated with metasurface frequency response and quality factor. As we can acquire the passive and active spectral reflectance of the QC-metasurface, we are able to calculate the multiplication of gain and fitting coefficient $\xi(\upsilon)g(\upsilon)$. If we can also measure the reference reflectance with a mirror as the sample, we will get gain $g(\upsilon)$ and fitting coefficient $\xi(\upsilon)$ separately. This requires the mirror to have exact same position and orientation as the metasurface. We plan to leave a certain area of the wafer not etched beside the metasurface so that the Ti/Au surface can act as a mirror, and this will be one of our future goals.

As for the electrical connection, we use synchronous double modulation to increase SNR[12]. The optical setup and electrical scheme are shown in Figure 3.4 while the biasing scheme and signal output from balanced detector are shown in Figure 3.5. The metasurface was cooled to 77 K and biased with 1 μs pulses at *f* = 10 kHz (1% duty cycle). The PCA was synchronously biased at *2f* = 20 kHz with 25% duty cycle, such that the QC-metasurface is only biased during every other pulse of the PCA.

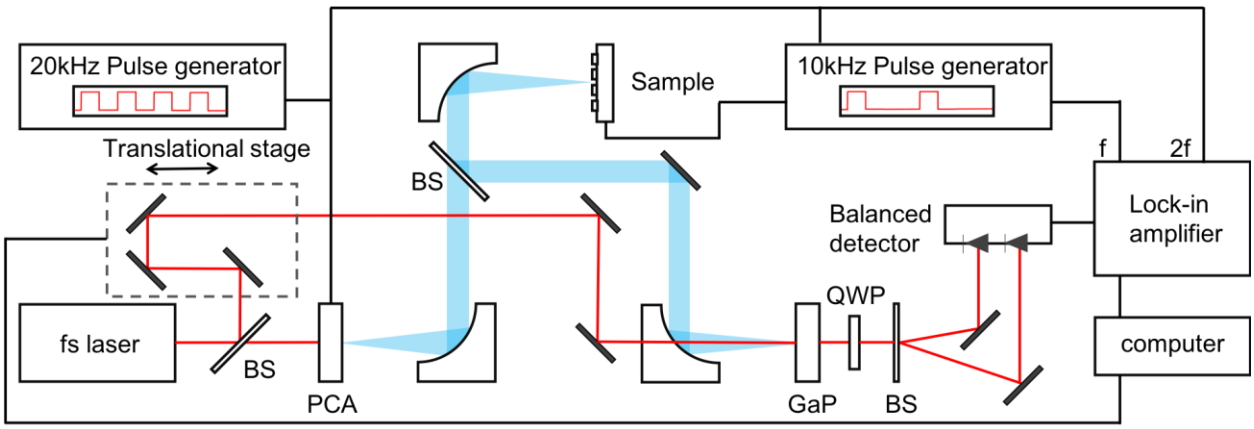

Figure 3.4 The schematic of THz TDS for active measurements of QC-metasurface.

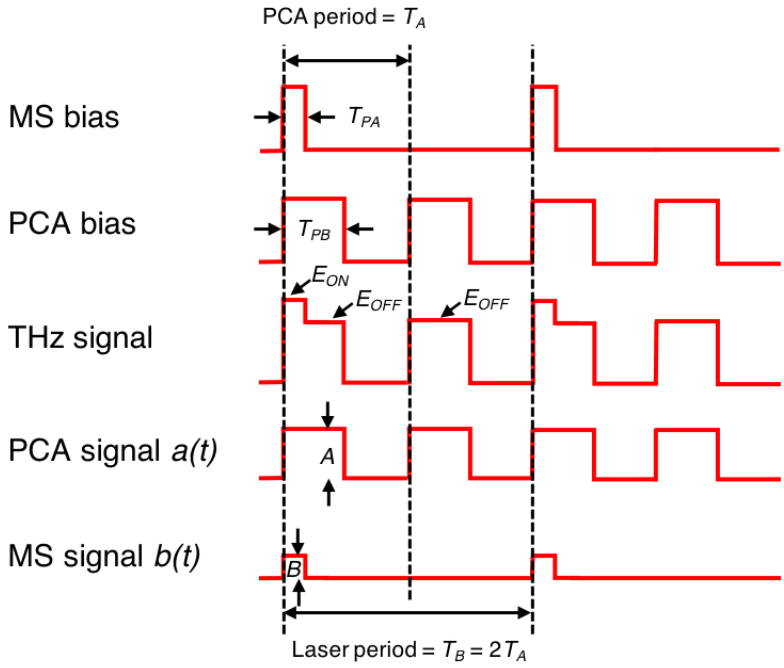

Figure 3.5 Biasing scheme and signal output for synchronous double modulation.

The total THz signal detected by the balanced detector can be regarded as the sum of *a(t)*, signal correlated with antenna, and *b(t)*, signal correlated with metasurface. The magnitude of *a(t)*, *A*, equals to E_{off} while the magnitude of *b(t)*, *B*, equals to $E_{on} - E_{off}$.

According to Fourier series expansion, *a(t)* and *b(t)* can be expressed as

$$a(t) = \frac{A(t) \cdot T_{PA}}{T_A} + \sum_{n=1}^{\infty} \frac{2A(t)}{n\pi} \sin\left(n\pi \frac{T_{PA}}{T_A}\right) \cos\left(n \frac{2\pi}{T_A}(t - t_0)\right), \tag{3.4}$$

$$b(t) = \frac{B(t) \cdot T_{PB}}{T_B} + \sum_{n=1}^{\infty} \frac{2B(t)}{n\pi} \sin\left(n\pi \frac{T_{PB}}{T_B}\right) \cos\left(n \frac{2\pi}{T_B}(t - t_0)\right). \tag{3.5}$$

As the sum of *a(t)* and *b(t)* are the output of balanced detector, which is also input of lock-in amplifier, we can pick out strength of lock-in signal at *f* = 10 kHz (S_f) and *2f* = 20 kHz (S_{2f}) separately and apply Fourier transformation.

$$S_f(\upsilon) = \frac{2B(\upsilon)}{\pi} \sin\left(\pi \frac{T_{PB}}{T_B}\right) \tag{3.6}$$

$$S_{2f}(\upsilon) = \frac{2A(\upsilon)}{\pi} \sin\left(\pi \frac{T_{PA}}{T_A}\right) + \frac{B(\upsilon)}{\pi} \sin\left(2\pi \frac{T_{PB}}{T_B}\right) \tag{3.7}$$

And thus, the division of E_{on} over E_{off} is

$$\frac{E_{on}(\upsilon)}{E_{off}(\upsilon)} = \frac{B(\upsilon)}{A(\upsilon)} + 1 = \frac{2\sin\left(\pi \frac{T_{PB}}{T_B}\right) S_{2f}(\upsilon) + \left[2\sin\left(\pi \frac{T_{PA}}{T_A}\right) - \sin\left(2\pi \frac{T_{PB}}{T_B}\right)\right] S_f(\upsilon)}{2\sin\left(\pi \frac{T_{PB}}{T_B}\right) S_{2f}(\upsilon) - \sin\left(2\pi \frac{T_{PB}}{T_B}\right) S_f(\upsilon)}. \tag{3.8}$$

Due to the low duty cycle of the QC-bias, lock-in detection at frequency *2f* gives a spectral density $\left|S_{2f}(\upsilon)\right|^2$ that is dominated by the reflection of the entire TDS pulse from the passive metasurface, while lock-in detection at *f* retrieves the differential reflection spectral density $\left|S_f(\upsilon)\right|^2$ – which is proportional to the metasurface gain[88].

The simulation result of metasurface reflectance is shown in Figure 3.6. Our goal is to build the relationship between gain and laser bias by comparing the simulation reflectance and experimental reflectance. The experimental results of active measurements are shown in Figure 3.7. By comparing the temporal electric field demodulated at *f* = 10kHz and *2f* = 20kHz (Figure 3.7a and b), we can find the amplified oscillation (2 - 6 ps in E_f) as a result of gain from metasurface, while E_{2f} is mostly dominated by the characteristics of passive metasurface. This metasurface is known to provide gain, since in a separate experiment, when an output coupler mirror was added lasing

was observed in a VECSEL configuration with threshold current density of J_{th} = 1070 A/cm^2 (current I = 3 A) at 77K. We can tell the lasing region in the inset of Figure 3.7c as it is associated with a change in slope of the I-V characteristic due to the onset of stimulated emission assisted transport within the active region. The metasurface absorption associated with the passive metasurface is observed as a strong dip at 2.6 THz in $\left|S_{2f}(\upsilon)\right|^2$, almost the same as the passive measurements. When metasurface is biased with J = 1100 A/cm^2, narrowband amplification (resolution limited) is observed at the expected frequency of 2.6 THz, as seen in $\left|S_{f}(\upsilon)\right|^2$. For comparison, this signature is absent for a low bias of J = 27 A/cm^2.

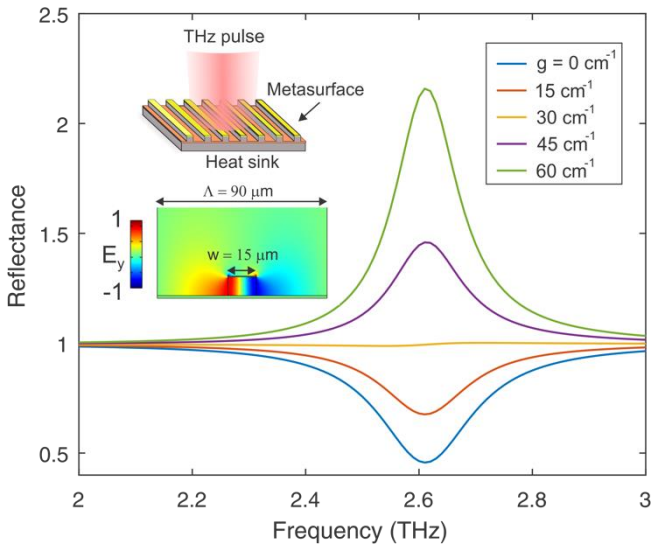

Figure 3.6 Reflectance simulation of QC-metasurface with different intersubband gain. Electric field of metal-metal waveguide ridge and interaction between free space THz pulse and QC-metasurface is shown in the inset.

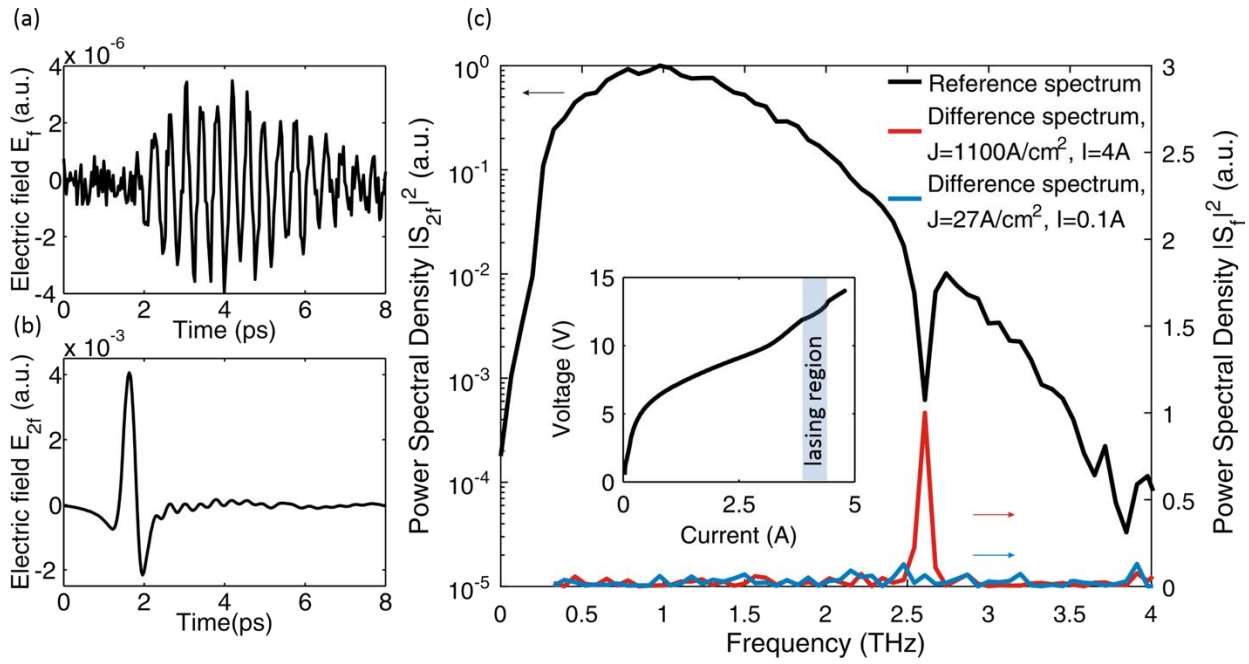

Figure 3.7 (a) The electric field of signal demodulated at frequency f = 10 kHz when metasurface is biased with current 2.8 A. (b) The electric field of signal demodulated at $2f$ = 20 kHz with same bias for metasurface. (c) The black curve $|S_{2f}(v)|2$ shows mainly the passive reflectance of QC metasurface, while the red and blue curves depict differential reflectance $|S_f(v)|^2$ associated with the metasurface bias. The V-I curve of VECSEL tested with the addition of an output coupler is shown in the inset.

3.3 Conclusion

We have demonstrated the first characterization of an active THz QC metasurface using THz TDS for the first time. We have shown a signature of resonant reflectance modulation at 2.6 THz, which is consistent our simulations and with FTIR measurements of a QC-VECSEL fabricated using similar metasurfaces. We strongly believe that this is a signature of gain from the metasurface, in particular since the same metasurface biased in a VECSEL configuration showed lasing behavior. However, we are not yet able to quantitatively measure the absolute reflectance gain spectrum. This is due to the fact that the absorption of the passive spectrum is so strong

compared to the gain that the active material can provide. When substitute the experimental parameter into Eq. 3-8, we can get the result $\frac{E_{on}(\upsilon)}{E_{off}(\upsilon)} = 1 + 22.5 * \frac{S_f}{S_{2f} - S_f}$. Due to the strong absorption at 2.6 THz, the magnitude of S_{2f} is 2 to 3 orders larger than S_f. Thus, the calculated gain spectra may seem weird that the bandwidth is much narrower than the simulations. Increasing the duty cycle for the bias of metasurface or find another metasurface sample with less absorption may help to solve the problem.

As says in prior paragraphs, the reflection from substrate of the emitter is limiting the resolution of characterization in frequency domain. To solve the problem, we are trying numerical methods to eliminate the echoes. We are also considering fabricating the PCA with LT-GaAs using an echoless design in the future. The purpose is to broaden the bandwidth and eliminate the reflections from the substrate/air interface. As for the challenge caused by the low duty cycle of the metasurface bias and the strong absorption of the metasurface, we are fabricating new metasurface at 2.7 and 2.3 THz right now. We expect the metasurface to be of large size so it's easier to focus the THz beam onto the metasurface. We also need the duty cycle to be as high as possible. As low duty cycle is necessitated by the large current draw of the metasurface, smaller area metasurfaces will enable higher duty cycles. As our requirements, high duty cycle and large size, are contradictory, we make several designs of the metasurface from smaller size to larger one. There will be an optimized one that enables higher duty cycle while still providing a large radiating aperture to couple efficiently to the incident THz signal. Once those problems are solved, we hope to extract $\frac{E_{on}(\upsilon)}{E_{off}(\upsilon)}$ under different operating conditions, like difference bias and different temperature. We also expect to extract the phase spectra from measurements. Once the bandwidth

of emission from PCA is extended to 4 THz, we can try to characterize some broadband metasurface at high frequency (3.4 THz) and investigate the group delay dispersion (GDD).

Appendix A: Experimental Procedures

A.1 Buildup of THz TDS system

The real setup of the TDS system is shown in Figure A.1, which is the realization of the schematic in Figure 2.2. The purple line indicates the ultrafast laser beam coming from a Spectra-Physics Tsunami femtosecond laser. It is split into a pump beam (blue line) and a probe beam (orange line) at the optical beam splitter. The pump beam irradiates onto the PCA (depicted in the inset) to generate THz beam (red line). The buildup of the TDS system started from choosing appropriate devices to aligning the optical paths. The tips and tricks accumulated during the process of setting up a system are listed below.

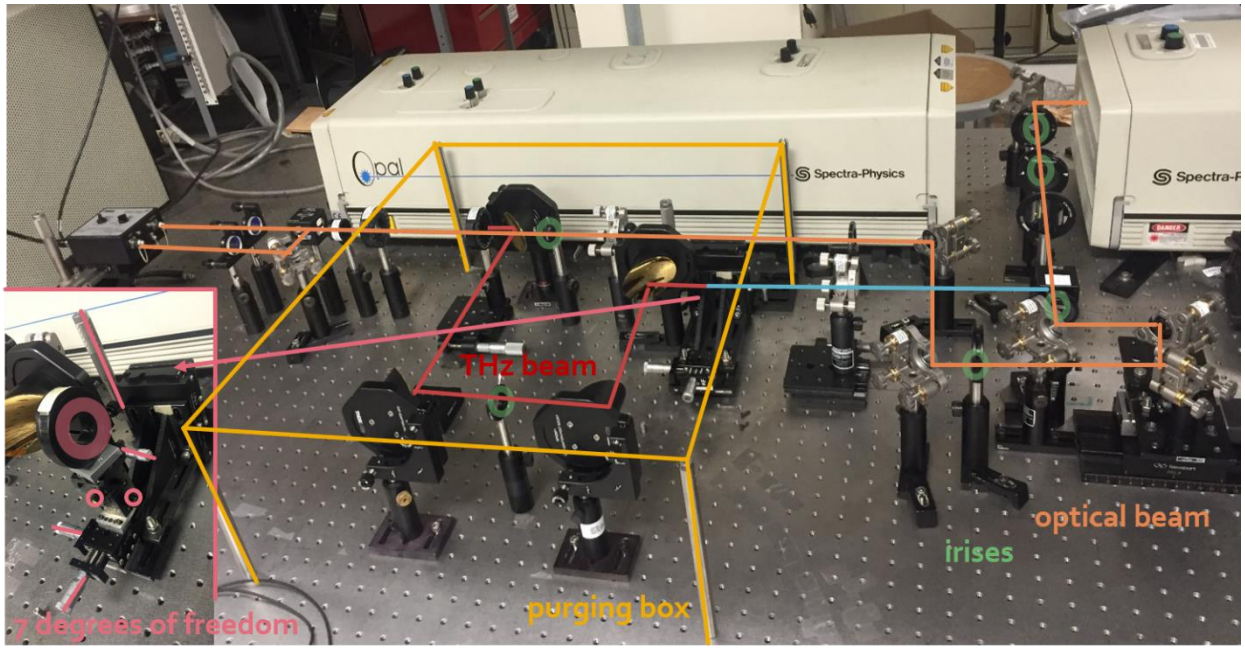

Figure A.1 Picture of the real THz TDS system.

a) The holes on the optical table are helpful for alignment if their positions coincide with the center of the optical elements horizontally, as they can give us the reference of the beam direction. Thus, we try to screw the post holders directly onto the optical table without bases or clamps. As for the kinematic mounts of mirrors, we prefer the ones that have the post-mounting holes aligned with front surface of mirror to simplify alignment.

b) The irises (green circles in Figure A.1) are fully utilized in my setup. During the process of buildup, two irises are used to make sure the optical beams are parallel to the lines of holes on the optical table. Also, in many critical positions, irises are screwed there to make sure the beam doesn't steer away in a long run. This is especially important as our lab is in Los Angeles where earthquakes are common.

c) For specific optical elements, like the PCA, the optical lens in front of the PCA, the first off-axis parabolic mirror, the last off-axis parabolic mirror, the sample, together with the added mirror and THz beamsplitter for reflection mode, I try to add as much degrees of freedom to adjust as possible for better alignment(inset of Figure A.1 and Figure A.2). For the PCA in inset of Figure A.1, there are optomechanical components to grant seven degrees of freedom to control: a rotational mount, a 3-axises translational stage, two horizontally tilting stages and a rotational stage. As for other cases as shown in Figure A.2, translational stages are the most common components to be added to hold the optical elements.

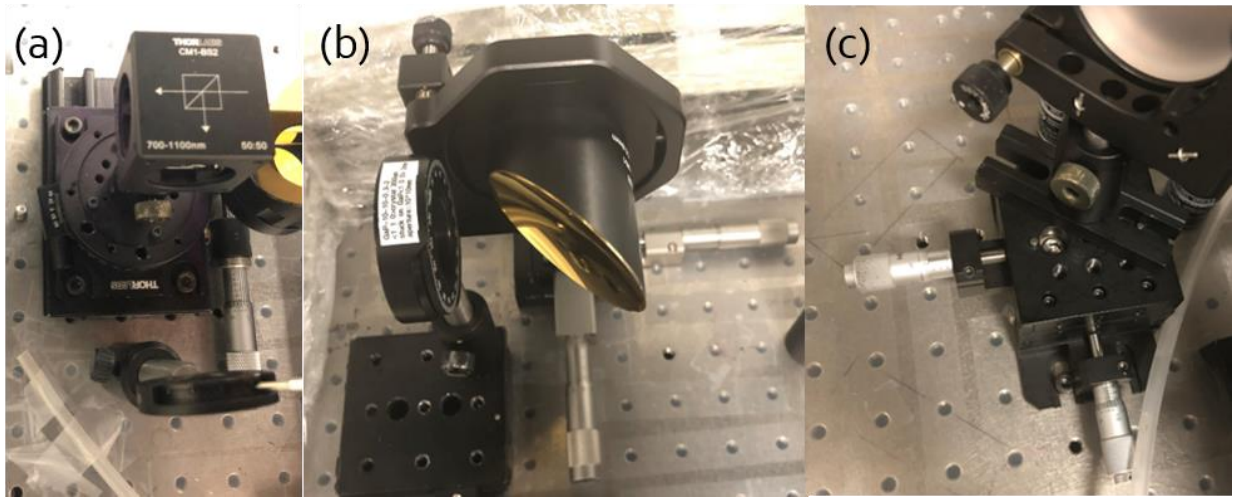

Figure A.2 Examples of some optical elements with more degrees of freedom to adjust.

d) The most difficult part of the alignments is the guidance of the THz beam path as we cannot see the THz beam. We solved this problem by adding a flip mount for the PCA. Thus, during alignments, the PCA is flipped away from optical beam path so that the optical beam can be regarded as the THz beam. And we can tune the orientation of the off-axis parabolic mirrors to make sure the optical beam can reach the expected destination.

e) As the sample needs to be placed inside the cryostat and the cryostat requires the 3-axis translational stage in the base, we introduce the periscopes to raise the beam vertically to match the position of samples (Figure A.3).

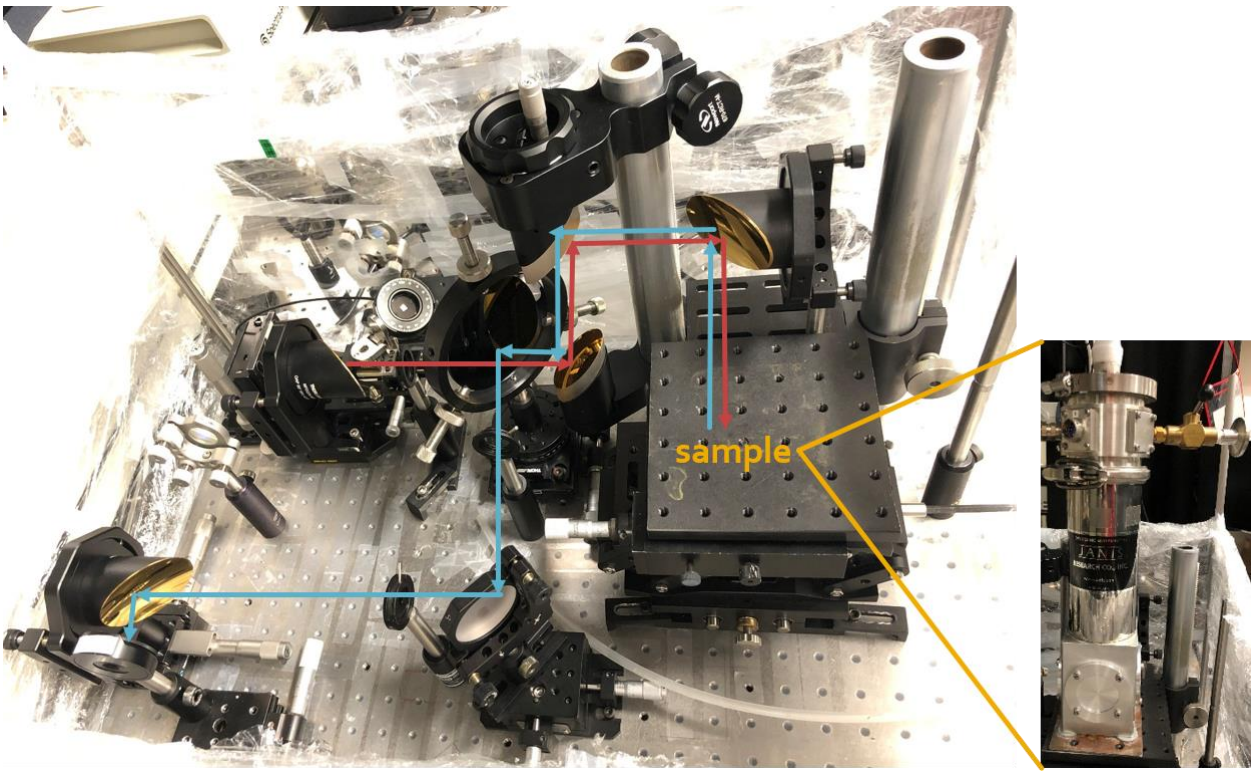

Figure A.3 The picture of the reflection mode setup inside the purging box.

f) As the size of metasurface is only 1.5 mm * 1.5 mm, it's important to make sure that we are shining the THz beam only on the target sample. As says in prior paragraph that we cannot see the THz beam path, focusing THz beam onto the metasurface is challenging. The schematic of the sample is shown in Figure A.4. The surface of the wafer and the surface of the copper holder have some height difference. We can use the height difference to find the target metasurface. For surfaces with different height, the peak value of the reflected THz signal corresponds to different time, and the time difference is roughly double wafer thickness divided by speed of light. With help of the translational stage, we can find the bottom left corner of the wafer by verifying the reflected characteristics of copper holder disappear when the sample is moved down or

left. After finding the bottom left corner, it's easy to focus THz beam onto metasurface by moving the sample down or left step by step and verify that the dip at 2.6 THz in the spectra is deepest.

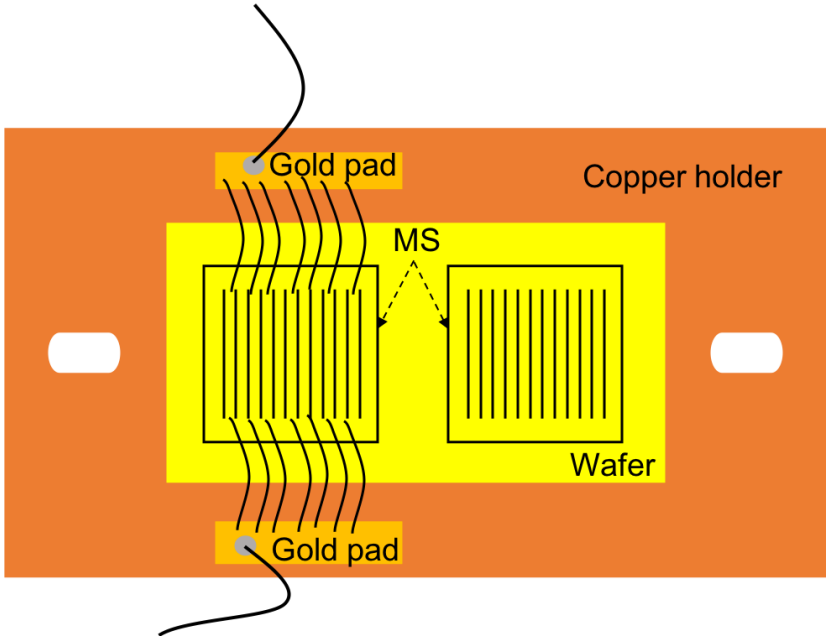

Figure A.4 Schematic of the sample.

g) We need to be aware of the following three conditions that might cause damage to the PCA: dielectric breakdown, damage caused by high laser intensity and damage caused by ohmic heating. To prevent dielectric breakdown, we can keep the bias voltage below 50 V. To solve the high laser intensity issue, we control the laser power under 600 mW and ensure the spot-size to be around 300 μm (radius) by tuning the relative distance between the lens and the PCA and verifying with knife-edge experiment. As for the ohmic heating problem, we need to monitor the average current and bias voltage to make sure the product of average current and voltage is kept below 0.75W. Thus, we design

a new way for electrical connection (shown in Figure A.5) to monitor the average current and bias voltage at any time.

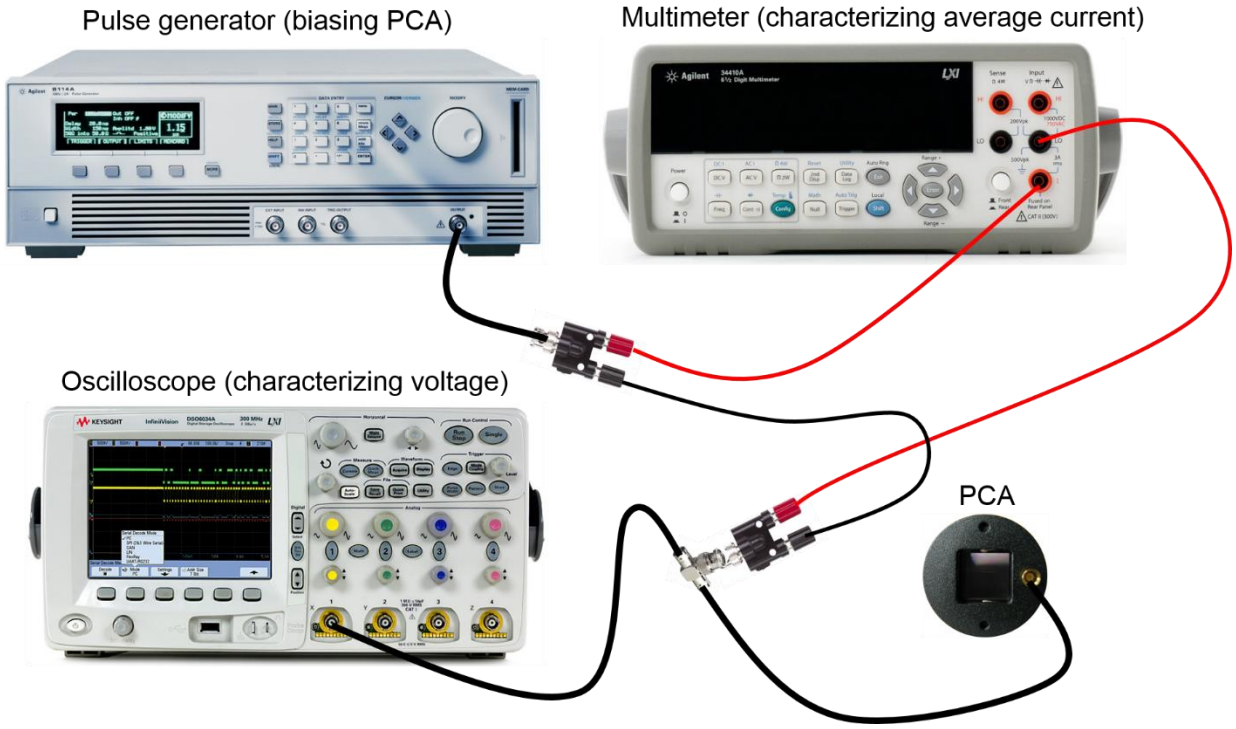

Figure A.5 Schematic of the electrical connection for the PCA.

A.2 Maintenance of the femtosecond laser

Femtosecond laser is the key component of the THz TDS system. Thus, the maintenance and daily operation of the femtosecond laser (shown in Figure A.6) needs great care. The operating procedure of the femtosecond laser is listed below:

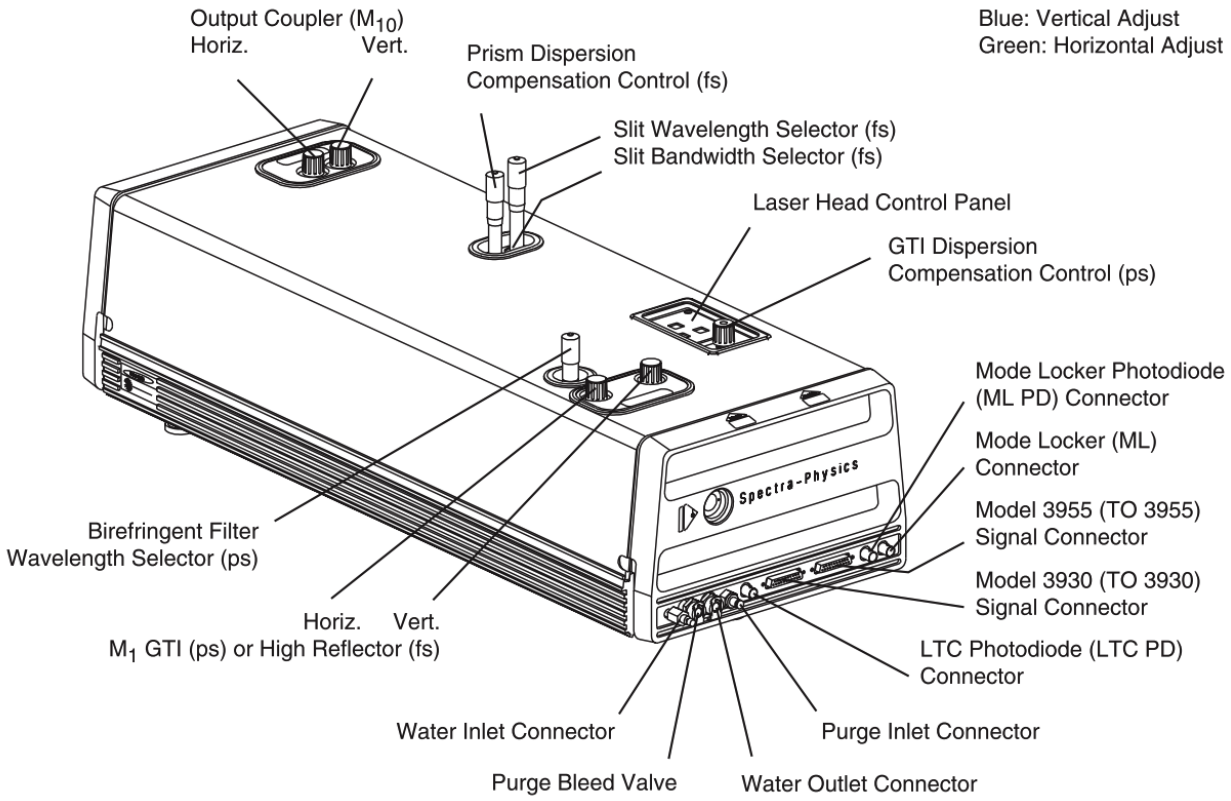

Figure A.6 Tsunami femtosecond laser external laser head (This figure courtesy of User's Manual of Tsunami Mode-locked Ti:sapphire Laser).

a) Press the "LASER POWER" on the controller for 3 seconds to start the laser.

b) Press "P2" to set pump power to 10W.

c) After 30 minutes, check module 3955 to see whether the signal light of "PULSING" is on. If not, use thick slab to cover the Tsunami output window until the light of "PULSING" is on.

d) Place a power meter in front of the Tsunami laser. Tune M10 and M1 slightly to optimize the output power to maximum.

e) Use the spectrometer to check the pulse width is 12 nm and the center frequency is around 800 nm.

References

1. Köhler, R., Tredicucci, A., Beltram, F., Beere, H. E., Linfield, E. H., Davies, A. G., Ritchie, D. A., Iotti, R. C. & Rossi, F. Terahertz semiconductor-heterostructure laser. *Nature* **417**, 156 (2002).

2. Williams, B. S. Terahertz quantum-cascade lasers. *Nat. Photonics* **1**, 517–525 (2007).

3. Williams, B. S., Kumar, S., Hu, Q. & Reno, J. L. Operation of terahertz quantum-cascade lasers at 164 K in pulsed mode and at 117 K in continuous-wave mode. *Opt. Express* **13**, 3331 (2005).

4. Williams, B. S., Kumar, S., Hu, Q. & Reno, J. L. High-power terahertz quantum cascade lasers. *Electron. Lett.* **42**, 89 (2006).

5. Li, L., Chen, L., Zhu, J., Freeman, J., Dean, P., Valavanis, A. & Linfield, E. H. Terahertz quantum cascade lasers with >1 W output powers. *Electron. Lett.* **50**, 309–311 (2014).

6. Vitiello, M. S., Scalari, G., Williams, B. S., De Natale, P. & DeNatale, P. Quantum cascade lasers: 20 years of challenges. *Opt. Express* **23**, 5167 (2015).

7. Auston, D. H., Cheung, K. P., Valdmanis, J. A. & Kleinman, D. A. Cherenkov radiation from femtosecond optical pulses in electro-optic media. *Phys. Rev. Lett.* **53**, 1555–1558 (1984).

8. Wu, Q. & Zhang, X. ‐C. Ultrafast electro ‐optic field sensors. *Appl. Phys. Lett.* **68**, 1604–1606 (1996).

9. Wu, Q., Hewitt, T. D. & Zhang, X. ‐C. Two ‐dimensional electro ‐optic imaging of THz beams. *Appl. Phys. Lett.* **69**, 1026–1028 (1996).

10. Kröll, J., Darmo, J., Dhillon, S. S., Marcadet, X., Calligaro, M., Sirtori, C. & Unterrainer, K. Phase-resolved measurements of stimulated emission in a laser. *Nature* **449**, 698–701 (2007).

11. Kröll, J., Darmo, J., Unterrainer, K., Dhillon, S. S., Sirtori, C., Marcadet, X. & Calligaro, M. Longitudinal spatial hole burning in terahertz quantum cascade lasers. *Appl. Phys. Lett.* **91**, 161108 (2007).

12. Jukam, N., Dhillon, S., Zhao, Z. Y. Z.-Y. Z. Y., Duerr, G., Armijo, J., Sirmons, N., Hameau, S., Barbieri, S., Filloux, P., Sirtori, C., Marcadet, X. & Tignon, J. Gain measurements of THz quantum cascade lasers using THz time-domain spectroscopy. *IEEE J. Sel. Top. Quantum Electron.* **14**, 436–442 (2008).

13. Jukam, N., Dhillon, S. S., Oustinov, D., Zhao, Z. Y., Hameau, S., Tignon, J., Barbieri, S., Vasanelli, A., Filloux, P., Sirtori, C. & Marcadet, X. Investigation of spectral gain narrowing in quantum cascade lasers using terahertz time domain spectroscopy. *Appl. Phys. Lett.* **93**, 91–94 (2008).

14. Jukam, N. *et al.* Terahertz time domain spectroscopy of phonon-depopulation based quantum cascade lasers. *AIP Conf. Proc.* **1399**, 369–370 (2009).

15. Rungsawang, R. *et al.* Integrated terahertz pulse generation and amplification in quantum cascade lasers. *Appl. Phys. Lett.* **96**, 983–984 (2010).

16. Burghoff, D., Kao, T. Y., Ban, D., Lee, A. W. M., Hu, Q. & Reno, J. A terahertz pulse emitter monolithically integrated with a quantum cascade laser. *Appl. Phys. Lett.* **98**, 3–5 (2011).

17. Martl, M., Darmo, J., Deutsch, C., Brandstetter, M., Andrews, A. M., Klang, P. & Strasser, G. Gain and losses in THz quantum cascade laser with metal-metal waveguide. *Opt. Express* **19**, 733–738 (2011).

18. Lloyd-Hughes, J., Scalari, G., van Kolck, A., Fischer, M., Beck, M. & Faist, J. Coupling terahertz radiation between sub-wavelength metal-metal waveguides and free space using monolithically integrated horn antennae. *Opt. Express* **17**, 18387 (2009).

19. Lee, A. W. M., Qin, Q., Kumar, S., Williams, B. S., Hu, Q. & Reno, J. L. High-power and high-temperature THz quantum-cascade lasers based on lens-coupled metal-metal waveguides. *Opt. Lett.* **32**, 2840–2842 (2007).

20. Yu, N., Wang, Q. J., Kats, M. A., Fan, J. A., Khanna, S. P., Li, L., Davies, A. G., Linfield, E. H. & Capasso, F. Designer spoof surface plasmon structures collimate terahertz laser beams. *Nat. Mater.* **9**, 730–735 (2010).

21. Oustinov, D. *et al.* Phase seeding of a terahertz quantum cascade laser. *Nat. Commun.* **1**, (2010).

22. Maysonnave, J., Jukam, N., Ibrahim, M. S. M., Maussang, K., Madéo, J., Cavalié, P., Dean, P., Khanna, S. P., Steenson, D. P., Linfield, E. H., Davies, A. G., Tignon, J. & Dhillon, S. S. Integrated injection seeded terahertz source and amplifier for time-domain spectroscopy. *Opt. Lett.* **37**, 731 (2012).

23. Bachmann, D., Leder, N., Rösch, M., Scalari, G., Beck, M., Arthaber, H., Faist, J., Unterrainer, K. & Darmo, J. Broadband terahertz amplification in a heterogeneous quantum cascade laser. *Opt. Express* **23**, 3117 (2015).

24. Jukam, N., Dhillon, S. S., Oustinov, D., Madeo, J., Manquest, C., Barbieri, S., Sirtori, C., Khanna, S. P., Linfield, E. H., Davies, A. G. & Tignon, J. Terahertz amplifier based on gain switching in a quantum cascade laser. *Nat. Photonics* **3**, 715–719 (2009).

25. Maysonnave, J., Jukam, N., Ibrahim, M. S. M., Rungsawang, R., Maussang, K., Madéo, J., Cavalié, P., Dean, P., Khanna, S. P., Steenson, D. P., Linfield, E. H., Davies, A. G. & Dhillon, S. S. Measuring the sampling coherence of a terahertz quantum cascade laser. *Opt. Express* **20**, 16662–16670 (2012).

26. Nong, H., Pal, S., Markmann, S., Hekmat, N., Mohandas, R. A., Dean, P., Li, L., Linfield, E. H., Giles Davies, A., Wieck, A. D., Jukam, N., Davies, A. G., Wieck, A. D. & Jukam, N. Narrow-band injection seeding of a terahertz frequency quantum cascade laser: Selection and suppression of longitudinal modes. *Appl. Phys. Lett.* **105**, 111113 (2014).

27. Wang, C. Y., Kuznetsova, L., Gkortsas, V. M., Diehl, L., Kartner, F. X., Belkin, M. A., Belyanin, A., Li, X., Ham, D., Schneider, H., Grant, P., Song, C. Y., Haffouz, S., Wasilewski, Z. R., Liu, H. C. & Capasso, F. Mode-locked pulses from mid-infrared Quantum Cascade Lasers. *Opt. Express* **17**, 12929–12943 (2009).

28. Barbieri, S., Ravaro, M., Gellie, P., Santarelli, G., Manquest, C., Sirtori, C., Khanna, S. P., Linfield, E. H., Davies, A. G., Manques, C., Sirtori, C., Khanna, S. P., Linfield, E. H. &

Davies, A. G. Coherent sampling of active mode-locked terahertz quantum cascade lasers and frequency synthesis. *Nat. Photon.* **5**, 306–313 (2011).

29. Freeman, J. R., Maysonnave, J., Jukam, N., Cavalié, P., Maussang, K., Beere, H. E., Ritchie, D. A., Mangeney, J., Dhillon, S. S. & Tignon, J. Direct intensity sampling of a modelocked terahertz quantum cascade laser. *Appl. Phys. Lett.* **101**, 181115 (2012).

30. Maysonnave, J., Maussang, K., Freeman, J. R., Jukam, N., Madéo, J., Cavalié, P., Rungsawang, R., Khanna, S. P., Linfield, E. H., Davies, A. G., Beere, H. E., Ritchie, D. A., Dhillon, S. S. & Tignon, J. Mode-locking of a terahertz laser by direct phase synchronization. *Opt. Express* **20**, 20855–20862 (2012).

31. Freeman, J. R., Maysonnave, J., Beere, H. E., Ritchie, D. A., Tignon, J. & Dhillon, S. S. Electric field sampling of modelocked pulses from a quantum cascade laser. *Opt. Express* **21**, 16162 (2013).

32. Wang, F., Nong, H., Fobbe, T., Pistore, V., Houver, S., Markmann, S., Jukam, N., Amanti, M., Sirtori, C., Moumdji, S., Colombelli, R., Li, L., Linfield, E., Davies, G., Mangeney, J., Tignon, J. & Dhillon, S. Short Terahertz Pulse Generation from a Dispersion Compensated Modelocked Semiconductor Laser. *Laser Photonics Rev.* **11**, 1–9 (2017).

33. Giesen, A., Hügel, H., Voss, A., Wittig, K., Brauch, U. & Opower, H. Scalable concept for diode-pumped high-power solid-state lasers. *Appl. Phys. B* **58**, 365–372 (1994).

34. Kuznetsov, M., Hakimi, F., Sprague, R. & Mooradian, A. High-Power (0.5-W CW) Diode-Pumped Vertical-External-Cavity Surface-Emitting Semiconductor Lasers with Circular TEM Beams. *IEEE Photon. Tech. Lett.* **9**, 1063–1065 (1997).

35. Tropper, A. C., Foreman, H. D., Garnache, A., Wilcox, K. G. & Hoogland, S. H. Vertical-external-cavity semiconductor lasers. *J. Phys. D. Appl. Phys.* **37**, R75–R85 (2004).

36. Rudin, B., Rutz, A., Hoffmann, M., Maas, D. J. H. C., Bellancourt, A.-R., Gini, E., Südmeyer, T. & Keller, U. Highly efficient optically pumped vertical-emitting semiconductor laser with more than 20 W average output power in a fundamental transverse mode. *Opt. Lett.* **33**, 2719–2721 (2008).

37. Xu, L., Curwen, C. A., Chen, D., Reno, J. L., Itoh, T. & Williams, B. S. Terahertz metasurface quantum-cascade VECSELs: Theory and performance. *IEEE J. Sel. Top. Quantum Electron.* **23**, 1200512 (2017).

38. Xu, L., Curwen, C. A., Hon, P. W. C., Chen, Q.-S., Itoh, T. & Williams, B. S. Metasurface external cavity laser. *Appl. Phys. Lett.* **107**, 221105 (2015).

39. Xu, L., Chen, D., Itoh, T., Reno, J. L. & Williams, B. S. Focusing metasurface quantum-cascade laser with a near diffraction-limited beam. *Opt. Express* **24**, 24117–24128 (2016).

40. Xu, L., Chen, D., Curwen, C. A., Memarian, M., Reno, J. L., Itoh, T. & Williams, B. S. Metasurface quantum-cascade laser with electrically switchable polarization. *Optica* **4**, 468–475 (2017).

41. Jepsen, P. U., Cooke, D. G. & Koch, M. Terahertz spectroscopy and imaging – Modern techniques and applications Peter. *Laser Photonics Rev.* **5**, 124–166 (2011).

42. Waters, J. W. Submillimeter-Wavelength Heterodyne Spectroscopy and Remote Sensing of the Upper Atmosphere. *Proc. IEEE* **80**, 1679–1701 (1992).

43. Groeneveld, R. H. M. & Grischkowsky, D. Picosecond time-resolved far-infrared experiments on carriers and excitons in GaAs-AlGaAs multiple quantum wells. *J. Opt. Soc. Am. B* **11**, 2502 (1994).

44. Kaindl, R. A., Carnahan, M. A., Hägele, D., Lövenich, R. & Chemla, D. S. Ultrafast terahertz probes of transient conducting and insulating phases in an electron–hole gas. *Nature* **423**, 734–738 (2003).

45. Leinß, S., Kampfrath, T., v.Volkmann, K., Wolf, M., Steiner, J. T., Kira, M., Koch, S. W., Leitenstorfer, A. & Huber, R. Terahertz Coherent Control of Optically Dark Paraexcitons in Cu 2 O. *Phys. Rev. Lett.* **101**, 246401 (2008).

46. Matthew C. Beard, Gordon M. Turner, and & Schmuttenmaer*, C. A. Measuring Intramolecular Charge Transfer via Coherent Generation of THz Radiation. (2002). doi:10.1021/JP013603L

47. Whitmire, S. E., Wolpert, D., Markelz, A. G., Hillebrecht, J. R., Galan, J. & Birge, R. R. Protein Flexibility and Conformational State: A Comparison of Collective Vibrational Modes of Wild-Type and D96N Bacteriorhodopsin. *Biophys. J.* **85**, 1269–1277 (2003).

48. He, Y., Ku, P. I., Knab, J. R., Chen, J. Y. & Markelz, A. G. Protein Dynamical Transition Does Not Require Protein Structure. *Phys. Rev. Lett.* **101**, 178103 (2008).

49. Winnewisser, C., Lewen, F. & Helm, H. Transmission characteristics of dichroic filters measured by THz time-domain spectroscopy. *Appl. Phys. A Mater. Sci. Process.* **66**, 593–598 (1998).

50. Wilk, R., Vieweg, N., Kopschinski, O. & Koch, M. Liquid crystal based electrically switchable Bragg structure for THz waves. *Opt. Express* **17**, 7377 (2009).

51. Jansen, C., Wietzke, S., Astley, V., Mittleman, D. M. & Koch, M. Mechanically flexible polymeric compound one-dimensional photonic crystals for terahertz frequencies. *Appl. Phys. Lett.* **96**, 111108 (2010).

52. Griffiths, P. R. *Fourier Transform Infrared Spectrometry (FTIR)*. **222**, (Wiley-Interscience, 2015).

53. Exter, M., Fattinger, C. & Grischkowsky, D. Terahertz time-domain spectroscopy of water vapor. *Opt. Lett.* **14**, 1128–30 (1989).

54. Han, P. Y., Tani, M., Usami, M., Kono, S., Kersting, R. & Zhang, X. C. A direct comparison between terahertz time-domain spectroscopy and far-infrared Fourier transform spectroscopy. *J. Appl. Phys.* **89**, 2357–2359 (2001).

55. Auston, D. H. Subpicosecond electro-optic shock waves. *Appl. Phys. Lett.* **43**, 713–715 (1983).

56. Auston, D. H., Cheung, K. P. & Smith, P. R. Picosecond photoconducting Hertzian dipoles. *Appl. Phys. Lett.* **45**, 284–286 (1984).

57. Ketchen, M. B., Grischkowsky, D., Chen, T. C., Chi, C. C., Duling, I. N., Halas, N. J., Halbout, J. M., Kash, J. A. & Li, G. P. Generation of subpicosecond electrical pulses on coplanar transmission lines. *Appl. Phys. Lett. Appl. Phys. Lett.* **48**, 751–753 (1986).

58. Fattinger, C. & Grischkowsky, D. Point source terahertz optics. *Appl. Phys. Lett.* **53**, 1480–1482 (1988).

59. Fattinger, C. & Grischkowsky, D. Terahertz beams. *Appl. Phys. Lett.* **54**, 490–492 (1989).

60. Auston, D. H. H. & Nuss, M. C. C. Electrooptic generation and detection of femtosecond electrical transients. *IEEE J. Quantum Electron.* **24**, 184 (1988).

61. Jepsen, P. U., Jacobsen, R. H. & Keiding, S. R. Generation and detection of terahertz pulses from biased semiconductor antennas. *J. Opt. Soc. Am. B* **13**, 2424 (2008).

62. Madéo, J., Jukam, N., Oustinov, D., Rosticher, M., Rungsawang, R., Tignon, J., Dhillon, S. S. S., Madeo, J., Jukam, N., Oustinov, D., Rosticher, M., Rungsawang, R., Tignon, J. & Dhillon, S. S. S. Frequency tunable terahertz interdigitated photoconductive antennas. *Electron. Lett.* **46**, 611 (2010).

63. Yardimci, N. T. & Jarrahi, M. High Sensitivity Terahertz Detection through Large-Area Plasmonic Nano-Antenna Arrays. *Sci. Rep.* **7**, 42667 (2017).

64. Burford, N. M. & El-Shenawee, M. O. Review of terahertz photoconductive antenna technology. *Opt. Eng.* **56**, 010901 (2017).

65. Jackson, J. D. *Classical electrodynamics*. (Wiley, 1962).

66. Němec, H., Pashkin, A., Kužel, P., Khazan, M., Schnüll, S. & Wilke, I. Carrier dynamics in low-temperature grown GaAs studied by terahertz emission spectroscopy. *J. Appl. Phys.* **90**, 1303–1306 (2001).

67. Moreno, E., Pantoja, M. F., Garcia, S. G., Bretones, A. R. & Martin, R. G. Time-Domain Numerical Modeling of THz Photoconductive Antennas. *IEEE Trans. Terahertz Sci. Technol.* **4**, 490–500 (2014).

68. Tani, M., Lee, K.-S. & Zhang, X.-C. Detection of terahertz radiation with low-temperature-grown GaAs-based photoconductive antenna using 1.55 μm probe. *Appl. Phys. Lett.* **77**, 1396–1398 (2000).

69. Shen, Y. C., Upadhya, P. C., Linfield, E. H., Beere, H. E. & Davies, A. G. Ultrabroadband terahertz radiation from low-temperature-grown GaAs photoconductive emitters. *Appl. Phys. Lett.* **83**, 3117–3119 (2003).

70. Shen, Y. C., Upadhya, P. C., Beere, H. E., Linfield, E. H., Davies, A. G., Gregory, I. S., Baker, C., Tribe, W. R. & Evans, M. J. Generation and detection of ultrabroadband terahertz radiation using photoconductive emitters and receivers. *Appl. Phys. Lett.* **85**, 164–166 (2004).

71. Chou, S. Y., Liu, Y. & Fischer, P. B. Tera‐hertz GaAs metal‐semiconductor‐metal photodetectors with 25 nm finger spacing and finger width. *Appl. Phys. Lett.* **61**, 477–479 (1992).

72. Yardimci, N. T., Yang, S.-H., Berry, C. W. & Jarrahi, M. High-Power Terahertz Generation Using Large-Area Plasmonic Photoconductive Emitters. *IEEE Trans. Terahertz Sci. Technol.* **5**, 223–229 (2015).

73. Dreyhaupt, A., Winnerl, S., Dekorsy, T. & Helm, M. High-intensity terahertz radiation from a microstructured large-area photoconductor. *Appl. Phys. Lett.* **86**, 1–3 (2005).

74. Liu, L., Hesler, J. L., Xu, H., Lichtenberger, A. W. & Weikle, R. M. A broadband quasi-optical terahertz detector utilizing a zero bias Schottky diode. *IEEE Microw. Wirel. Components Lett.* **20**, 504–506 (2010).

75. Zhang, W., Khosropanah, P., Gao, J. R., Kollberg, E. L., Yngvesson, K. S., Bansal, T., Barends, R. & Klapwijk, T. M. Quantum noise in a terahertz hot electron bolometer mixer. *Appl. Phys. Lett.* **96**, 111113 (2010).

76. Wu, Q. & Zhang, X. ‐C. Free ‐space electro ‐optic sampling of terahertz beams. *Appl. Phys. Lett.* **67**, 3523–3525 (1995).

77. Nahata, A., Weling, A. S. & Heinz, T. F. A wideband coherent terahertz spectroscopy system using optical rectification and electro-optic sampling. *Appl. Phys. Lett.* **69**, 2321–2323 (1996).

78. Nahata, A., Auston, D. H., Heinz, T. F. & Wu, C. Coherent detection of freely propagating terahertz radiation by electro ‐optic sampling. *Appl. Phys. Lett.* **68**, 150–152 (1996).

79. Liu, J.-M. *Principles of Photonics*. *Principles of Photonics* (2016). doi:10.1017/cbo9781316687109

80. Wu, Q. & Zhang, X.-C. X.-C. 7 terahertz broadband GaP electro-optic sensor. *Appl. Phys. Lett.* **70**, 1784–1786 (1997).

81. Darmo, J., Martl, M. & Unterrainer, K. Quasi phase-matched terahertz detector. *Electron. Lett.* **46**, 788 (2010).

82. Kübler, C., Huber, R. & Leitenstorfer, A. Ultrabroadband terahertz pulses: generation and field-resolved detection. *Semicond. Sci. Technol.* **20**, S128–S133 (2005).

83. Schneider, A., Neis, M., Stillhart, M., Ruiz, B., Khan, R. U. A. & Günter, P. Generation of terahertz pulses through optical rectification in organic DAST crystals: theory and experiment. *J. Opt. Soc. Am. B* **23**, 1822 (2006).

84. Van Der Valk, N. C. J., Schouten, R. N. & Planken, P. C. M. Noise suppression of a differential detector under high levels of illumination, relevant to terahertz electro-optic sampling. *Rev. Sci. Instrum.* **76**, 1–6 (2005).

85. Jepsen, P. U. & Fischer, B. M. Dynamic range in terahertz time-domain transmission and reflection spectroscopy. *Opt. Lett.* **30**, 29–31 (2005).

86. Maussang, K., Brewer, A., Palomo, J., Manceau, J. M., Colombelli, R., Sagnes, I., Mangeney, J., Tignon, J. & Dhillon, S. S. Echo-Less Photoconductive Antenna Sources for High-Resolution Terahertz Time-Domain Spectroscopy. *IEEE Trans. Terahertz Sci. Technol.* **6**, 20–25 (2016).

87. Maussang, K., Palomo, J., Manceau, J. M., Colombelli, R., Sagnes, I., Li, L. H., Linfield, E. H., Davies, A. G., Mangeney, J., Tignon, J. & Dhillon, S. S. Monolithic echo-less photoconductive switches for high-resolution terahertz time-domain spectroscopy. *Int. Conf. Infrared, Millimeter, Terahertz Waves, IRMMW-THz* **141102**, (2017).

88. Burghoff, D. P. Broadband terahertz photonics. (2014).